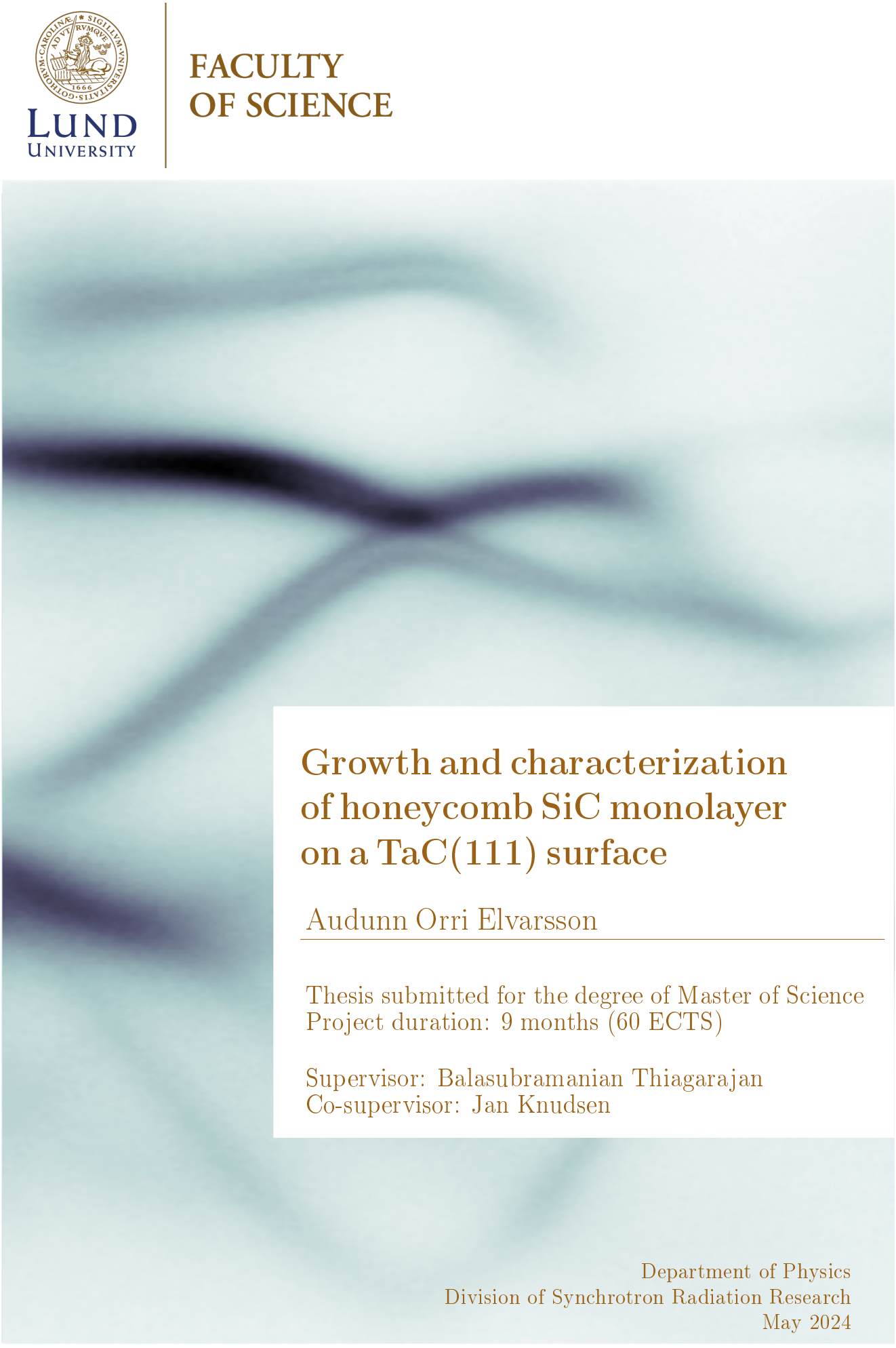

LUND UNIVERSITY

FACULTY OF SCIENCE

Growth and characterization of honeycomb SiC monolayer on a TaC(111) surface

Audunn Orri Elvarsson

Thesis submitted for the degree of Master of Science
Project duration: 9 months (60 ECTS)

Supervisor: Balasubramanian Thiagarajan
Co-supervisor: Jan Knudsen

Department of Physics
Division of Synchrotron Radiation Research
May 2024

Abstract

This thesis proves the successful synthesis of silicon carbide (SiC) monolayers on the tantalum carbide (TaC) (111) substrate through a novel bottom-up growth method, offering improved control over the supply of constituent materials for a more detailed study of the formation process. Initial examination of the clean TaC(111) surface revealed surface-induced states in its electronic band structure. Core level measurements of the Ta 4f core level distinguished its surface and bulk components, but the presence of two bulk peaks led to an investigation of the carbon concentration of the crystal. Analysis of carbon deposition dynamics on the TaC(111) surface revealed carbon diffusion into the bulk resulting in increased TaC stoichiometry. This stoichiometry enhancement was found to be essential to form a SiC monolayer. After silicon deposition, carbon diffused to the surface, bonding with silicon and forming 2D SiC, confirmed by comparing the measured band structure with DFT calculations. The ARPES measurements found that the 2D SiC interacts strongly with the TaC substrate through π band hybridization with the TaC surface states, resulting in a strongly spin-orbit split Dirac-like feature at the $\overline{K}$ points. Moreover, by depositing an excess amount of carbon, graphene forms on top of the TaC. After silicon deposition, 2D SiC forms underneath the graphene, making it more freestanding. Future research could examine the stability of the SiC monolayer in ambient environments and see whether graphene can provide any protective benefits. Additional next steps would be to explore proximity-induced superconductivity and intercalating layers beneath the SiC monolayer to decouple it from the substrate, allowing a more direct comparison with its theorized electronic properties. By demonstrating a novel and practical way of synthesizing large-area SiC monolayers, this thesis brings 2D SiC into the growing family of two-dimensional materials.

Popular science summary

By adding carbon and silicon to a tantalum carbide surface, my thesis reveals a new method of creating two-dimensional silicon carbide, a material that could lead to more efficient electronic devices.

Today's electronics rely heavily on silicon, as most people know. To improve our devices, these silicon electronics have been made smaller and smaller, but have now reached their limit. Imagine if instead of using bulky three-dimensional structures, we could use ultra-thin sheets of atoms stacked together. These sheets, known as *two-dimensional (2D) materials*, have sparked a new wave of research since the Nobel Prize-winning discovery of graphene in 2010. Graphene, a single layer of carbon atoms, showed us that 2D materials could revolutionize technology, but it has limitations.

For instance, graphene doesn't have a *band gap* — a property crucial for controlling the flow of electricity in devices like computers, where we need clear on/off states (like traffic lights managing the flow of cars). This band gap is essential for creating the binary ones (electric current) and zeros (no electric current) that are the foundation of computer logic. Materials with a band gap are called *semiconductors*, and those with a direct band gap are particularly useful for devices such as LEDs, lasers, and solar cells. A direct band gap is like a well-paved road that allows cars to accelerate smoothly and efficiently after stopping at a traffic light, while an indirect band gap is like a twisting road that makes cars take longer to reach full speed.

In my research, I focus on creating a new 2D material: silicon carbide (SiC), which combines silicon and carbon atoms in a single layer. Scientists believe that 2D SiC could be a game-changer because it has a direct band gap but making it has been very challenging. Recently, a breakthrough showed that heating a silicon carbide crystal with a thin layer of tantalum carbide (TaC) on top can help form 2D SiC.

Building on this discovery, my goal was to create 2D SiC directly on a TaC crystal. By adding carbon and silicon to a heated TaC surface, I successfully formed the 2D SiC. This method gave me better control over the formation process and deeper insights

into how 2D SiC grows. Additionally, by adjusting the amount of carbon, I could create a graphene layer on top of the 2D SiC. Graphene's stability raised the exciting possibility of using it as a protective layer over the 2D SiC. Future research could explore this possibility.

Most importantly, my work showed a new and controlled way of creating 2D SiC, bringing it closer to being used in the next generation of electronic and optical devices. This could lead to faster, more efficient technology, continuing the progress we've made with silicon but taking it to the next level.

Acknowledgments

I would like to express my heartfelt gratitude to my supervisor, Balasubramanian Thiagarajan, for his guidance and support throughout this project at MAX IV. Despite the initial challenges, his expertise, insightful discussions, and encouragement helped me overcome these problems and achieve our goal. A special thanks for your help with ARPES and core level measurements – your knowledge was invaluable.

A sincere appreciation to Jacek Osiecki for his instrumental role in setting up and maintaining the heating system for the preparation chamber. I'm deeply grateful for your patience in sharing your knowledge of the vacuum chambers and the sample preparation procedures with me, without it I doubt that this project would have been possible. I am also thankful for your time and assistance with the ARPES and core level measurements.

I extend my gratitude to Craig Polley for providing band structure calculations that proved essential to understanding the experimental data. Your collaboration and support with the ARPES and core level measurements were also immensely valuable and greatly appreciated.

I would like to thank Khadiza Ali for her thoughtful talks, ranging from core level fitting to life's philosophies and suffering.

To Mats Leandersson, Gerardina Carbone, and Hanna Fedderwitz, along with the rest of the aforementioned Bloch team members, I express my appreciation for their support and friendship throughout the project. Our weekly meetings where we (mostly I) shared jokes, memes, or bad buns made this experience more memorable and enjoyable.

I want to sincerely thank my co-supervisor Jan Knudsen, my examiner Mathieu Gisselbrecht, and my co-examiner Rainer Timm for their thorough reviews of my thesis and constructive criticism. I would also like to express my gratitude to Jan Knudsen for helping me gain access to Igor Pro, a software tool that was crucial for analyzing the data.

Lastly, I would like to recognize that ChatGPT helped me to review this paper. It pointed me to areas in my writing style that could be improved and offered advice on how to organize sentences and paragraphs. I have examined and validated any feedback that has been generated. The final draft of the paper is my own creation.

Contents

List of Figures

List of Tables

Abbreviations

ARPES	Angle-resolved photoelectron spectroscopy
cPGM	Collimated plane-grating monochromator
DFT	Density functional theory
EPU	Elliptically polarizing undulator
ES	Exit slit
FWHM	Full width at half maximum
LEED	Low-energy electron diffraction
ROI	Region of interest
SiC	Silicon carbide
STM	Scanning tunneling microscope
TaC	Tantalum carbide
TMC	Transition metal carbide
UHV	Ultra-high vacuum
XPS	X-ray photoelectron spectroscopy
XPST	X-ray Photoelectron Spectroscopy Tools

Chapter 1

Introduction

In the last decades, electronic devices have seen improved performance and reduced costs. This has largely been made possible by continuously making transistors and electronic components smaller and smaller. Now, these traditional silicon-based transistors have essentially reached their physical limit. To gain a marginal reduction in size, engineers face immense technical challenges [6]. To continue improving transistors, researchers have started exploring alternative device geometries and new channel materials, for which two-dimensional (2D) crystals hold promise. Their atomically thin dimension gives them new properties that are not found in their bulk counterparts. For example, charge carrier mobility, contact resistance, saturation velocity, critical electric field, and heat dissipation can change drastically [7]. These new qualities have the potential to improve the performance of transistors and other electronic devices at a lower power consumption [1, 7].

Examples of 2D materials that have been used in 2D transistors are graphene as the electrode [8], and hexagonal boron nitride as the insulator [9]. Commonly used as semiconductors are transition metal dichalcogenides monolayers, which have two chalcogen atoms for each transition-metal atom [10, 11]. One advantage of 2D semiconductors is that their band structure can be engineered by reassembling them layer by layer into intentionally designed heterostructures [12–14]. Moreover, because of the weak bonding between the layers, their lattices do not need to match. This opens up the door to an enormous amount of possible structures, each with unique properties and benefits. In this thesis, I aim to expand the list of 2D semiconductors by synthesizing a hexagonal silicon carbide (SiC) monolayer on top of a tantalum carbide (TaC) surface.

The family of 2D materials has a rich variety of electrical properties, such as superconductors, dielectrics, and high-mobility semiconductors [15–18]. For example, graphene and silicene, the 2D form of silicon, exhibit exceptionally high charge carrier mobility and initially showed potential for making electronic devices faster [19]. However, a shared limitation of both materials is their absence of a band gap, posing challenges in controlling current flow and thereby limiting their use in electronic devices [20]. A potential way to open up a band gap is to create 2D sheets made of binary compounds from either group IV or group III-V elements [21]. In the context of my research, I will be focusing on two-dimensional silicon carbide layers.

Bulk SiC is a commonly used semiconductor in high-power electronics and high-temperature applications due to its wide indirect band gap and excellent thermal properties [22]. However, when SiC is scaled down to a monolayer, it experiences quantum confinement in one spatial dimension, a phenomenon that leads to the transformation to a direct band gap [3]. Numerous theoretical studies have investigated the structure and

properties of 2D SiC. Employing first-principles calculations based on density functional theory (DFT), researchers predict that 2D SiC has a honeycomb structure with sp^2 bonds. These bonds give good thermal and chemical stability, making 2D SiC ideal for harsh and high-temperature environments [4, 21]. Calculations on free-standing 2D SiC predict that it has a direct band gap of approximately 2.5 eV [23–25]. The transition from an indirect to a direct band gap as SiC becomes atomically thin gives 2D SiC intriguing optical properties that could be used in optoelectronic devices [3]. These properties include pronounced photoluminescence and excitonic effects, which distinguish it from bulk SiC. As an indirect semiconductor, bulk SiC exhibits weak absorption and limited light-emitting qualities.

Two-dimensional SiC has not been implemented into devices yet because its practical synthesis has proven challenging due to the limitations of conventional top-down exfoliation methods. Unlike materials held together by weak van der Waals forces, bulk silicon carbide's robust sp^3 covalent bonding complicates the formation of a single monolayer. Overcoming this obstacle involves a demanding phase transformation from sp^3 to in-plane sp^2 bonding [3, 26]. However, a recent breakthrough by Polley et al. demonstrated the successful synthesis of a large-area honeycomb SiC monolayer. Their method, reminiscent of the epitaxial growth of graphene on SiC, consists of creating an ultrathin 111-terminated TaC film on a SiC substrate, followed by high-temperature annealing. This process not only reorders the carbide structure but also terminates the surface with a SiC monolayer [5].

These results laid the groundwork and inspiration for this thesis. In my project, the primary aim is to synthesize a SiC monolayer using a slightly different approach. Instead of having a thin TaC film on bulk SiC, a bulk TaC crystal with a 111-termination will be used as the substrate. The two main reasons for the use of a bulk TaC(111) substrate are that its surface lattice matches closely with lattice calculations of 2D SiC [5] and because, compared to ultrathin TaC films, bulk TaC crystals are simpler to produce (although they remain expensive) [27].

This thesis starts with a scientific background on tantalum carbide and two-dimensional silicon carbide in Chapter 2. Following this, in Chapter 3 I discuss the experimental techniques used in my work: X-ray photoelectron spectroscopy (XPS), angle-resolved photoemission spectroscopy (ARPES), and low-energy electron diffraction (LEED). Subsequently, in Chapter 4 I review synchrotron light generation, as well as the optics, performance characteristics, and end station layout of the Bloch beamline at MAX IV, where my research was conducted.

The preparation of the sample is presented in Chapter 5 of this thesis, followed by the results in Chapter 6. The results begin with a discussion of the electronic structure of the TaC(111) surface. I further explore the dynamics of carbon deposition on the TaC(111) surface, revealing changes in carbon composition within the bulk caused by ethylene exposure. This provides insights into the kinetics and mechanisms of SiC monolayer formation. Experimental measurements and theoretical calculations confirm the synthesis of a honeycomb SiC monolayer on the TaC(111) surface, as evidenced by the observed band structure. The successful 2D SiC synthesis allows for greater flexibility in testing various preparation configurations to explore the growth dynamics in more detail. Consequently, I experimented with depositing excess carbon and silicon, observing graphene formation on TaC(111) and its transformation upon silicon deposition. These findings improve our understanding of the stability and functionality of the materials involved. Following this is a discussion in Chapter 7 on the growth parameters as well as

discrepancies between these new observations and previously published data. The thesis concludes with a summary of the results and an outlook on future research direction in Chapters 8 and 9, respectively. In this thesis, I proved that it is possible to grow a SiC monolayer on the TaC(111) surface and presented the formation dynamics. This brings 2D SiC a step closer to real-world applications, such as in transistors or optoelectronic devices.

Chapter 2

Scientific background

2.1 Tantalum carbide

Tantalum carbide (TaC) is a transition metal carbide (TMC) with a rock salt crystal structure, depicted in Figure 2.1a. This is a cubic lattice with strong atomic bonds, resulting in its high melting point close to 4000 °C and a hardness comparable to that of diamond [28]. Furthermore, TaC, which is metallic, exhibits superconducting behavior at relatively high temperatures, with a critical temperature of 10.3 K [29].

The cubic form of TaC exists in a wide range of substoichiometric compositions, denoted as TaC_x, where x indicates the molar ratio of carbon to tantalum [30–32]. The stability window of TaC_x extends from perfect stoichiometry ($x = 1$) to approximately $x = 0.71 - 0.82$ [30–33]. The carbon content and lattice parameter of TaC_x is found to be affected by annealing time and temperature [30]. While bulk carbon content decreases with increasing annealing temperature, surface regions may experience transient enrichment due to carbon diffusing to the surface and subsequently escaping into the vacuum [34]. Empirical formulas derived by Kempter et al. [30] and Bowman et al. [31] provide insights into the relationship between the lattice constant and stoichiometry. These formulas, built on experimental measurements, demonstrate a linear relationship between the lattice constant and the C:Ta molar ratio. Kempter's formula yields a lattice constant of 4.4560 ± 0.0004 Å for stoichiometric TaC, while Bowman's approximation gives 4.457 ± 0.001 Å.

Investigations into different low-index tantalum carbide surfaces reveal how their properties vary. While both the TaC(100) and TaC(111) surfaces undergo relaxation, neither reconstruction nor faceting has been observed. Faceting has only been documented on the

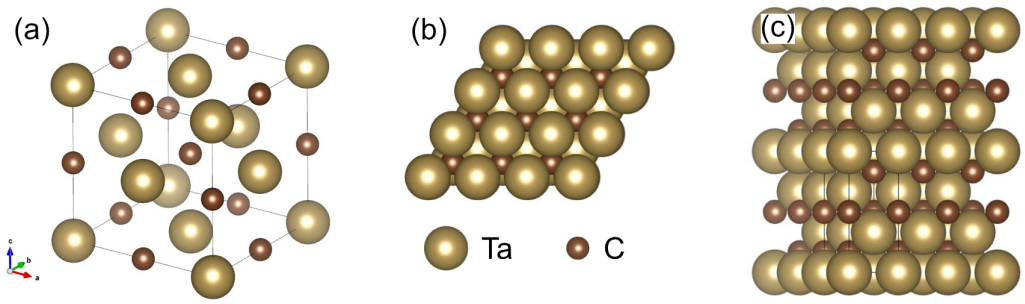

Figure 2.1: TaC crystal structure. (a) TaC unit cell. Top (b) and side (c) view of the TaC(111) surface.

(110) Ta surface, where the more energetically favorable (100) and (010) surfaces form in a hill-and-valley structure [35, 36]. Studies on the (111) surface of TaC, reveal a (1×1) hexagonal surface structure that usually terminates with the tantalum atoms [37–40]. The lattice constant of the TaC(111) surface is approximately 3.15 Å, as calculated from bulk values. A top and side view of the TaC(111) surface is shown in Figures 2.1b and 2.1c, respectively, demonstrating how the hexagonal layers form in alternating planes of Ta and C. The inherent instability of such polar surfaces has led to theoretical considerations of charge redistribution mechanisms to stabilize them. Theoretical models propose that the charge density increases in the first layer to counteract the long-range electric field [41]. This model has been experimentally validated for TaC(111), where surface-induced states were observed [38, 39, 42–45].

2.2 Two-dimensional silicon carbide

In recent years, interest in 2D materials has grown substantially, 2D SiC being one of them. Computational studies have found that 2D honeycomb Si_xC_{1-x} structures are potentially stable across a wide range of compositions (x) [3, 4, 46–51]. These predicted structures vary in stoichiometry and bonding configuration, offering a rich variety of test samples to explore 2D SiC properties. Additionally, adsorbents and defects such as vacancies, dopants, and grain boundaries can significantly influence 2D SiC properties, providing possibilities for customizing its behavior for specific applications [52–58]. Moreover, theoretical investigations have extended beyond 2D structures and into nanostructures, including SiC quantum dots, nanotubes, and nanowires [59, 60]. Among the 2D structures, stoichiometric SiC has been identified as the most stable [3].

In its most stable form, stoichiometric 2D SiC has a hexagonal lattice structure, with silicon and carbon atoms arranged in a honeycomb pattern as is shown in Figure 2.2a. This arrangement results in strong sp^2 hybridized covalent bonds between silicon and carbon atoms within the plane and a delocalized 4th electron, similar to graphene. Calculations and measurements report a lattice constant (C–C or Si–Si distance) in the range of $3.05 - 3.14$ Å for 2D SiC [5, 21, 23, 61–65]. Additionally, theoretical calculations of the band structure, shown in Figure 2.3a, indicate a direct band gap in the range of $2.40 - 2.58$ eV (or up to $3 - 4.8$ eV with special corrections and other approximations) between the π and π^* bands at the $\overline{K}$ symmetry point, making 2D SiC suitable for optoelectronic applications such as photodetection and light-emitting devices [5, 21, 23, 26, 61–65]. Notably, the theoretical direct band gap of 2D SiC stands in contrast to the indirect band gap of

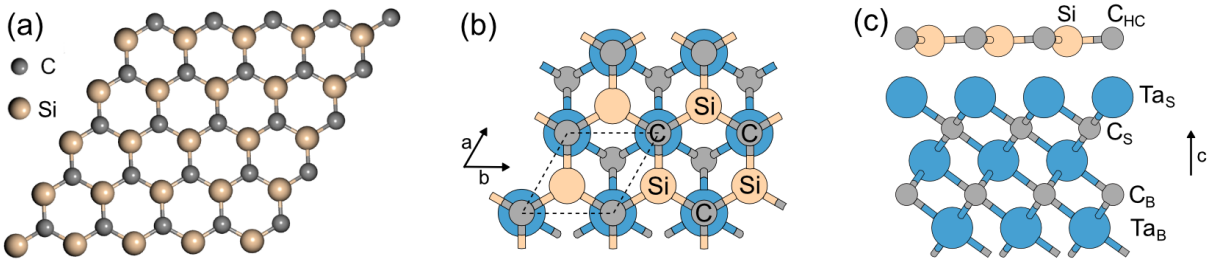

Figure 2.2: (a) Two-dimensional SiC lattice showing the honeycomb structure. Top (b) and side (c) view of the 2D SiC on top of the TaC(111) surface. The figures are drawn in accordance with the most likely explanation of measurement observations, with Si and C being on top of C and Ta, respectively, of the TaC substrate. Figures (b) and (c) are reproduced from [5].

its bulk counterpart.

Even though theoretical studies show the potential use of 2D SiC, its synthesis in the laboratory has proven challenging due to its strong inter-layered bonds. Unlike graphitic carbon, with its layered van der Waals structure, bulk SiC has strong covalent bonding between each layer, similar to silicon and diamond, requiring a phase transformation from sp^3 to sp^2 bonding to form a monolayer. This makes top-down mechanical exfoliation techniques especially difficult. Additionally, the existence of various SiC crystal structures complicates the formation of a 2D counterpart.

Despite these challenges, experimental efforts have made significant advancements that have resulted in the successful synthesis and preliminary characterization of 2D SiC. First, only nanosized grains of single or few layered SiC had been synthesized [26,64]. Chabi et al. then reported the synthesis of a fully planar honeycomb monolayer of SiC by employing a wet exfoliation method, albeit limited to small flakes [63]. This technique involves the mechanical separation of thin layers of 2D SiC from bulk crystals in a liquid medium, resulting in the formation of atomically thin flakes with minimal defects. Polley et al. then achieved the synthesis of large-area 2D SiC on a substrate using a new bottom-up approach [5]. In this method, an ultrathin transition metal carbide (TaC or NbC) film grown on 4H-SiC(0001) is subjected to controlled annealing, leading to the formation of a continuous 2D SiC layer through self-assembly processes over the whole sample surface. They hypothesize that Si and C atoms must have diffused from the SiC substrate and through the TaC film to form the SiC monolayer. This solves the problem of a direct sp^3 to sp^2 phase transformation. Instead, it happens in separate steps: first, the sp^3 bonds of the topmost atoms in the SiC substrate are broken, the Si and C atoms then diffuse through the TaC film and are finally free to bond in the now more energy efficient sp^2 bonds.

Building upon their synthesis methods, Polley et al. further investigated the structure and electronic properties of the 2D SiC [5]. Their results revealed that the C atoms are

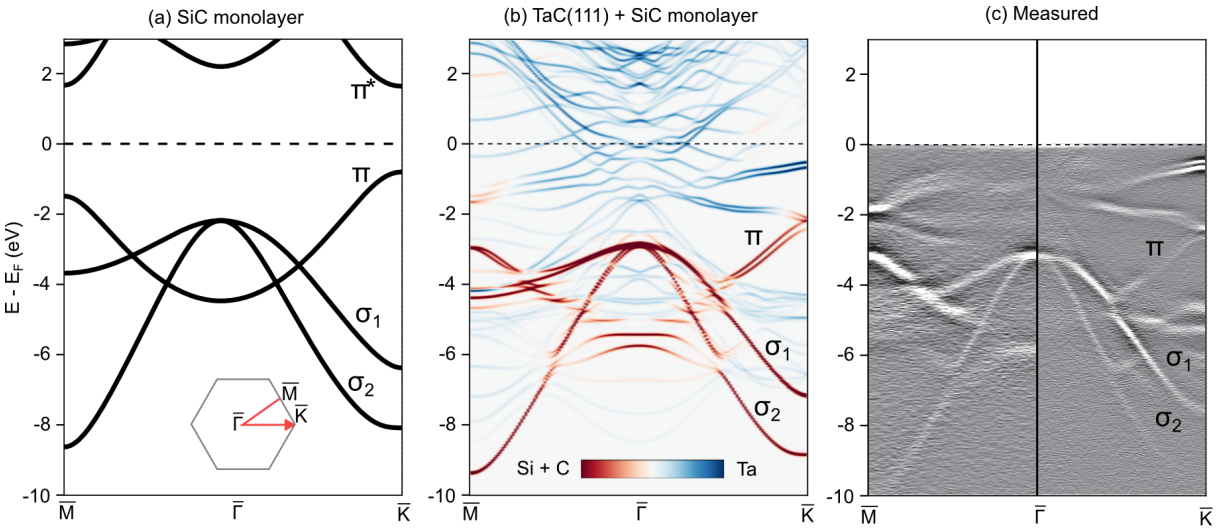

Figure 2.3: (a) DFT band structure calculations of a planar, freestanding SiC monolayer. The inset figure shows the path, $\overline{M}-\overline{\Gamma}-\overline{K}$, of the calculated band structure in the Brillouin zone. (b) The same calculation, now taking a Ta-terminated TaC(111) substrate into consideration (see Figs. 2.2b and 2.2c), sampling over the two topmost layers and resolving into atomic character. (c) Second derivative image of the measured band structure of Polley et al. along the same symmetry directions. These figures are reproduced from [5].

located atop the Ta atoms with the Si atoms in the hollow sites as seen in Figures 2.2b and c. They came to this conclusion after calculating the band structure of the SiC monolayer with the previously described structure, seen in Figure 2.3b, and observing an excellent agreement with the measured band structure, shown in Figure 2.3c. The calculated band structure was sampled over the two topmost layers and resolved into atomic character to see the contribution from the SiC layer and the TaC surface. These calculations are highly sensitive to the atomic positions of the modeled structure, thus serving as convincing evidence for the proposed atomic arrangement. They also found features in the electronic band structure such as a Dirac-like feature emerging due to the interaction between the SiC layer and the TaC substrate [5]. The band structure calculations and measurements demonstrate this interaction is caused by the hybridization of the π band of the SiC layer with the underlying Ta 5d orbitals.

Chapter 3

Experimental techniques

3.1 X-ray photoelectron spectroscopy of core levels

X-ray photoelectron spectroscopy (XPS) is a powerful analytical technique used for probing the elemental composition and chemical bonding of material surfaces [66–71]. In XPS, *core* electrons are studied and therefore the technique is often referred to as core level spectroscopy. Core electrons are tightly bound to the nucleus and therefore do not participate in chemical bonding, unlike valence electrons. XPS builds on the principle of the photoelectric effect, discovered by Einstein [72]. When a sample is irradiated with X-ray photons, core electrons are ejected from the atoms within the material. However, since electrons interact strongly with matter, only electrons from the topmost surface layers escape the sample without scattering or losing energy, making this technique surface sensitive. The kinetic energy (E_{kin}) of these emitted photoelectrons can be described by the equation:

$$E_{\text{kin}} = h\nu - \phi - E_{\text{B}}, \tag{3.1}$$

where $h\nu$ is the photon energy, E_{B} is the binding energy of the core electron, and ϕ is the work function of the material's surface, a measure of the potential barrier at the surface that electrons must overcome to escape. This equation illustrates how the kinetic energy of the emitted electrons directly correlates with the binding energy of the core electrons. These binding energies, unique to each element, serve as fingerprints for identifying the elemental composition of surface layers. Additionally, different chemical bonds and local atomic environments result in variations in core-electron binding energies, therefore giving information about the sample structure. Take for example crystalline silicon and SiO_2. The Si 2p core electron in pure silicon has a binding energy of about 99.3 eV. However, in SiO_2 the silicon valence electrons covalently bond with the oxygen, reducing the negative charge around the positively charged Si nucleus. This leads to the core electrons feeling a stronger pull of the nucleus which increases the binding energy of the Si 2p core electron to 103.3 eV [73]. Common core levels of interest, such as Si 2p, C 1s, and Ta 4f, are studied in my work to understand chemical bonding, oxidation states, and sample structure.

Curve fitting of core level spectra is an important part of XPS data analysis since one hereby can get qualitative information about the sample's composition and various chemical environments. Deconvolution of the spectra is achieved using curve fitting techniques, such as those implemented in the X-ray Photoelectron Spectroscopy Tools (XPST) package in Igor Pro, which is used in this study. First, the background signal is removed by fitting a Shirley background to address the inelastic scattering of photoelectrons [74–76].

As the X-rays strike the sample, they excite electrons to a final, virtual energy level.

This state decays exponentially in time leading to a Lorentzian contribution known as lifetime broadening [76]. The shape, measured by the analyzer, is additionally modified by instrumental broadening, giving rise to a Gaussian contribution. A convolution of the Gaussian and a Lorentzian function, known as a Voigt function, is often used to curve fit XP spectra.

The line shape used by the XPST package is a Gauss-Lorentzian sum function to approximate the Voigt profile, known as a Pseudo-Voigt (P-V) function [77]. This function accounts for the Gaussian and Lorentzian components and provides a suitable model for the asymmetric peak shapes often observed in XP spectra. It does this by introducing energy-dependent variations in the full width at half maximum (FWHM) parameter. The equations

$$\begin{aligned} \mathrm{P-V} &= (1-m)A\sqrt{\frac{4\ln 2}{\pi\omega_{(x)}^2}}\exp\left(-4\ln 2\left(\frac{x}{\omega_{(x)}}\right)^2\right) + m\frac{A}{2\pi}\frac{\omega_{(x)}}{\left(\omega_{(x)}/2\right)^2+x^2}, \\ \omega_{(x)} &= \frac{2\omega_0}{1+\exp\left(-ax\right)}, \qquad x = E - E_{\mathrm{peak}} \end{aligned} \tag{3.2}$$

describe the Pseudo-Voigt line shape as well as the asymmetry. The parameters of the function, which are detailed in Table 3.1, are refined through an iterative curve fitting, giving a quantitative description of the core level spectra.

In the context of my work, XPS is an important technique for understanding the surface composition and bonding configurations of the sample. By analyzing XPS spectra of Si, C, and Ta, I identify the presence of SiC layers, discern surface contaminants, and gain insights into the interaction between the SiC monolayer and the underlying TaC substrate, which is essential for understanding the growth process.

Table 3.1: Fitting parameters used in Eq. (3.2) to fit measured core levels.

Fit parameter	**Description**
A	Peak area
E_{peak}	Peak position (binding energy)
$\omega_{(x)}$	FWHM function
ω_0	FWHM parameter (actual FWHM for symmetric peaks)
m	Gauss-Lorentzian ratio (0 = Gaussian, 1 = Lorentzian)
a	Asymmetry parameter

3.2 Angle-resolved photoelectron spectroscopy

For crystals, angle-resolved photoemission spectroscopy (ARPES) is an effective technique to measure their band structure, which describes the energy-momentum relationship of electrons in the material, and thus provides important information on their electronic and optical properties [78–81]. ARPES not only measures the kinetic energy of emitted electrons like XPS but also directly probes the angle of emission, ϑ, thus determining their in-plane momentum.

As illustrated in Figure 3.1, the experimental setup typically involves a hemispherical electron analyzer. In this setup, emitted electrons pass through a multi-element electro-

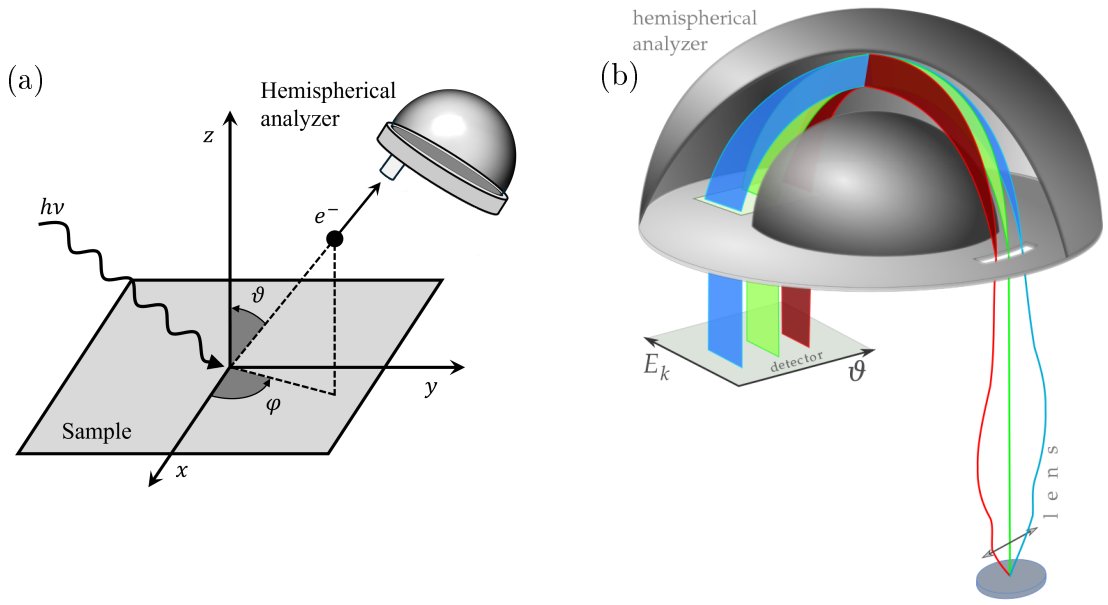

Figure 3.1: (a) Geometry of the ARPES setup and (b) a schematic of the hemispherical analyzer [82]. Electrons emitted at angles around ϑ are captured by the electron spectrometer. An electrostatic lens disperses the electrons along their emission angle. The hemispherical analyzer subsequently disperses the electrons by their kinetic energy, making the ARPES setup angle- and energy-resolving.

static lens which separates them according to their emission angle. A deflector controls which slice of the emitted angles passes into the analyzer, allowing for scanning the entire two-dimensional angle space. As the electrons pass into the hemispherical analyzer, through an entrance slit, they are already sorted according to their emission angles.

A potential difference (ΔV) between electronically isolated hemispheres with radii R_1 and R_2 then deflects the electrons radially based on their kinetic energy. By appropriately selecting ΔV, only electrons within a narrow range of kinetic energies, centered at the pass energy

$$E_{\text{pass}} = \frac{e\Delta V}{\frac{R_1}{R_2} - \frac{R_2}{R_1}}, \tag{3.3}$$

reach the detector [83]. The resolution of the kinetic energy is determined by the pass energy and the dimensions of the entrance slit w:

$$\Delta E_{\text{kin}} = E_{\text{pass}} \frac{w}{R_1 + R_2}. \tag{3.4}$$

Now that the kinetic energy is measured, Eq. (3.1) can be used to determine the binding energy of the electrons, since the photon energy is known and the work function of the material can be replaced by the work function of the analyzer. This is possible since the analyzer and sample are in electrical contact, and thus the kinetic energy of the electrons is measured relative to the analyzer work function.

From the angles and kinetic energy, the wavevector (or momentum) $\boldsymbol{k} = \boldsymbol{p}/\hbar$ of the photoelectrons in vacuum is fully determined [78]. The wavevector has a length $k = \sqrt{2mE_{\text{kin}}}/\hbar$ and components parallel, $\boldsymbol{k}_{\parallel}$, and perpendicular, $\boldsymbol{k}_{\perp}$, to the sample. These components are obtained in terms of the polar, ϑ, and azimuthal, φ, emission angles (see Fig. 3.1a). However, because the surface termination does not break the

in-plane translational symmetry but rather imposes an abrupt potential change normal to the surface, only the parallel component of the electron momentum is conserved [78], that is

$$k_{\parallel} = \frac{1}{\hbar}\sqrt{2mE_{\text{kin}}}\sin\vartheta. \tag{3.5}$$

To measure different directions in the $\boldsymbol{k}$-space, the azimuthal angle (φ) can be varied. Another way is to use a deflector which does not require rotation. As electrons get emitted from the sample, a cone of angles enters the electrostatic lenses but only a slice, determined by the deflector, enters the hemispherical analyzer. By continuously tilting the deflector, all of the different slices of the cone can be measured. By probing the electronic dispersion of the 2D SiC and TaC(111) surfaces using ARPES measurements, I can study their electronic properties in addition to the interaction between the layers through changes in the band structure.

3.3 Low-energy electron diffraction

Low-energy electron diffraction (LEED) is a technique used in surface science research to determine surface structures and symmetries [84–89]. It relies on the diffraction of low-energy electrons (typically in the range of $20 - 500\,\text{eV}$) from a crystalline surface to gain information about the arrangement of surface atoms. At these electron energies, their inelastic mean free path ranges from about 4 to 10 Å according to the universal curve [90]. At its most surface-sensitive kinetic energy ($\approx 40\,\text{eV}$), this would correspond to about three atomic layers of the TaC(111) surface (two Ta layers and one C layer).

In a typical LEED experiment, a beam of low-energy electrons is directed onto a clean single-crystal surface held under ultra-high vacuum conditions. As the electrons hit a crystalline surface, they undergo both elastic and inelastic scattering by the surface atoms [91–93]. The periodic arrangement of atoms in the crystal lattice results in constructive and destructive interference of the elastically scattered electrons, leading to the formation of diffraction spots that reflect the reciprocal lattice. These spots are then captured by a fluorescent screen positioned behind the electron gun. For my work in this thesis, the shape that these diffraction spots form can be used to gain information about the surface structure of the sample, including lattice constants and adsorbate arrangements. Moreover, by observing changes in the positions and intensities of these spots, we can gain insight into changes in the surface structure or the formation of new layers.

Chapter 4

Design and setup of the Bloch beamline

4.1 Synchrotron light generation at MAX IV

4.1.1 Storage ring

A storage ring is a circular particle accelerator used to store charged particles, which, in the case of MAX IV are electrons. MAX IV has two storage rings operating at 1.5 GeV and 3 GeV to cover a wide photon energy range [94]. A linear accelerator injects the electrons in short pulses with a duration below 100 fs into both storage rings. The electrons travel in a vacuum chamber that has magnetic bending and focusing elements that steer them into circular, nearly closed paths [95, 96]. The guide field focuses the electrons towards an ideal orbit, causing them to undergo radial and vertical oscillations (betatron oscillations) around this path. The system of magnetic lenses that guide and focus the electron beam is called the *lattice*. The choice of lattice determines the emittance, beam brightness, transverse coherence, beam lifetime, and the number of insertion devices that can be accommodated in the straight sections [94]. For the 1.5 GeV and 3 GeV rings, a double bend and 7 bend achromat lattices are used, resulting in a horizontal emittance of 6 nm rad and 0.3 nm rad, respectively [96]. These low emittances are essential to achieve a high brilliance. As the electrons circulate, they lose some energy through synchrotron radiation, which is then compensated by gaining energy from a radio frequency cavity or multiple cavities working together. Although both storage rings offer coherent and intense synchrotron radiation across a wide spectral range, the 1.5 GeV ring, where this thesis research is conducted, is specialized to provide better performances at low energies, where most surface science is performed.

4.1.2 Undulator

The synchrotron radiation used at MAX IV's experimental end stations is produced in insertion devices, either undulators or wigglers, located on the straight sections of the storage ring [96]. Both undulators and wigglers are made up of a periodic arrangement of magnet poles that causes the stored electron beam to oscillate transversely to the direction of motion of the beam and emits synchrotron radiation [97]. The Bloch beamline at MAX IV, where the research of this thesis is conducted, employs a quasi-periodic APPLE II (Q-APPLE II) type elliptically polarizing undulator (EPU) [98–100]. It consists of 28 periods of vertical and horizontal pairs of glued permanent magnets spanning a length of 2.6 m. With a period length of 84 mm and a minimum magnetic gap of 14 mm, it achieves

a minimum photon energy of 7.45 eV for horizontal linear polarization. Notably, the undulator offers horizontal, vertical, and circular polarization capabilities, making it adaptable to a broad range of experimental techniques. The beam size achieved at the center of the Bloch insertion device measures 185 µm × 13 µm (horizontal and vertical lengths, respectively). Additionally, adopting a quasi-periodic magnet configuration shifts higher harmonics away from integer multiples so they do not pass through the monochromator. This helps reduce higher-order contamination of the photon beam at the cost of a slightly reduced intensity of the first harmonic [101].

Important to understanding the undulator's performance and spectral properties is its strength parameter, defined as

$$K = \frac{e\lambda_u B_0}{2\pi m_e c}, \tag{4.1}$$

where λ_u is the undulator period, B_0 is the peak field of a sinusoidal magnetic field on the undulator axis, e is the electron charge, m_e is the electron rest mass, and c is the speed of light in vacuum [97]. This parameter correlates the peak field with the electron momentum, and by varying B_0, which is usually done by adjusting the magnetic gap, it is possible to change the resonance wavelengths [96]. Consequently, it influences the energy and polarization characteristics of the generated photon beam. If K is small, the oscillation amplitude of the motion is small, and the radiation displays interference patterns that lead to narrow energy bands. Conversely, for large K, the oscillation amplitude is large, resulting in a broader spectrum of emitted radiation. In this case, the device is called a wiggler. As mentioned before, Eq. (4.1) assumes a sinusoidal magnetic field. However, since the Q-APPLE II undulator has a non-sinusoidal magnetic field, the peak strength, B_0 is replaced by an effective magnetic field, B_{eff}. With $B_{\text{eff}} = 1.10\,\text{T}$, the effective strength of the Q-APPLE II undulator is $K_{\text{eff}} = 8.65$ [98]. During the design and construction of the undulator, these parameters were chosen to offer optimized performance for ARPES measurements in the lower photon energy range.

4.2 Bloch beamline optics

This section discusses the optical layout of the Bloch beamline, including mirrors and the monochromator, depicted in the schematic overview in Figure 4.1. While the beamline offers a photon energy range of 10 to 1000 eV, these optical elements offer optimal operation at under 220 eV [99–101]. Additionally, performance metrics such as energy resolution, photon flux, and spot size are discussed.

4.2.1 Optical elements

M1 - toroidal mirror Positioned 14 meters after the source, M1 serves as the first optical element, collimating the beam vertically and focusing it horizontally onto the exit slit, designed to manage the bulk of the heat load.

Monochromator The Bloch beamline utilizes a collimated plane-grating monochromator (cPGM), positioned two meters after M1, which introduces a vertical beam offset of 42 mm. The monochromator offers several grating options, but the one used in my work is the 800 L/mm (lines per millimeter) grating.

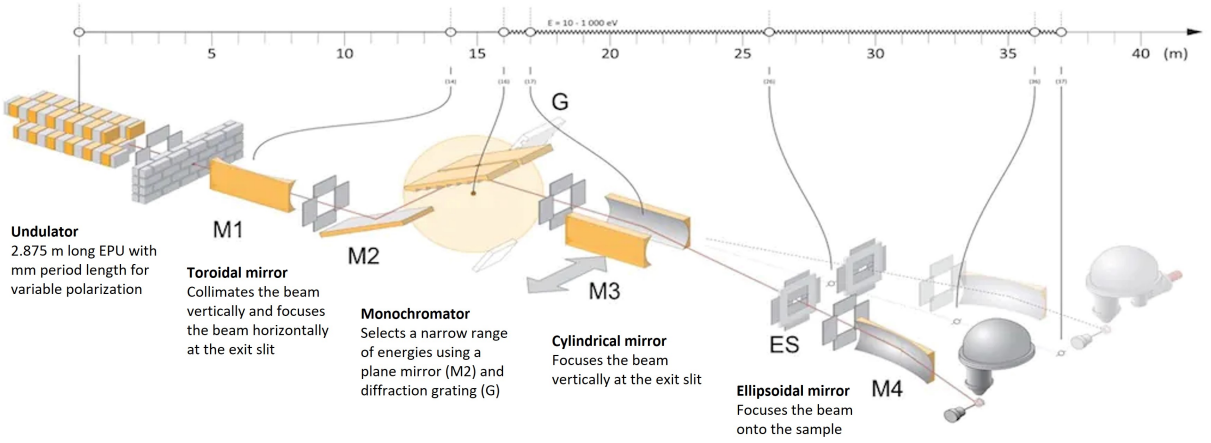

Figure 4.1: A schematic image of the optical layout of the Bloch beamline and the distances between the components. The X-ray is generated by a quasi-periodic elliptically polarizing undulator (EPU). M denotes the different optical mirrors, G is the grating used on the monochromator, and ES is the exit slit. The image is taken from [99].

M3 - cylindrical mirrors Positioned one meter after the monochromator, M3a and M3b are cylindrical mirrors that focus the beam vertically onto the exit slit of branch A and branch B, respectively.

Exit slits The exit slits of both branch lines, positioned 10.2 m after the M3 mirrors, regulate the energy resolution, total flux, and beam size by adjusting the horizontal and vertical slit openings and their longitudinal position along the beam.

M4 - ellipsoidal mirrors The final optical elements on each branch line, M4a/b, positioned 10 m after the exit slit, refocus the diverging beam leaving the exit slit to the sample position in the analysis chamber with a demagnification of 10:1.

4.2.2 Performance characteristics

Energy resolution The Bloch beamline's energy resolution is determined by multiple factors, including, but not limited to, the photon energy, the grating, and the exit slit width. The total energy resolution can be described in terms of the resolution due to the beam source ΔE_{S} and the exit slit ΔE_{slit} as [102]

$$\Delta E = \sqrt{\Delta E_{\mathrm{S}}^2 + \Delta E_{\mathrm{slit}}^2}. \tag{4.2}$$

The resolution due to the exit slit exhibits a linear dependence with its width. Consequently, at wider openings, the energy resolution is primarily determined by the slit width. However, the beam source resolution is independent of the exit slits, being primarily defined by the electron and photon source widths. Therefore, at small slit width, the total resolution becomes diffraction-limited due to the photon source size. This is clearly illustrated in Figure 4.2a, where the analytical equation (Eq. 4.2) of the total beamline resolution is plotted only as a function of the exit slit width, and other parameters are kept fixed. Reducing the slit width to improve the energy resolution is therefore only useful up to a limit, at which minimal improvements are obtained at a significant cost of beam intensity. Moreover, the resolution is roughly proportional to the square of

the photon energy. The expected resolution in the standard mode of operation, based on ray-tracing, is shown in Figure 4.2b for two exit slit widths. Under specific conditions, the beamline can reach an energy resolution of 1 meV at 21 eV or 2 meV at 63 eV. Higher resolution can be obtained by adjusting the grating or the monochromator configuration, albeit at the cost of intensity.

Photon flux Photon flux at the Bloch beamline ranges from 10^{10} to 10^{13} photons per second depending on energy resolution, spot size, and photon energy choice. Figure 4.3 illustrates flux variation with photon energy and experimental settings. With a minimum spot size of 100 µm × 100 µm, flux can be increased by approximately fourfold by widening the vertical exit slit gap to 800 µm. Below 200 eV, flux follows the first harmonic of the undulator, while above this value, the undulator gap closes to a fixed value, utilizing its broadband wiggler-mode output.

Spot size The Bloch beamline delivers a minimum photon spot size of 8 × 10 µm at normal incidence. However, since most samples are measured closer to normal emission than normal incidence, the horizontal footprint of the beam on the sample is typically

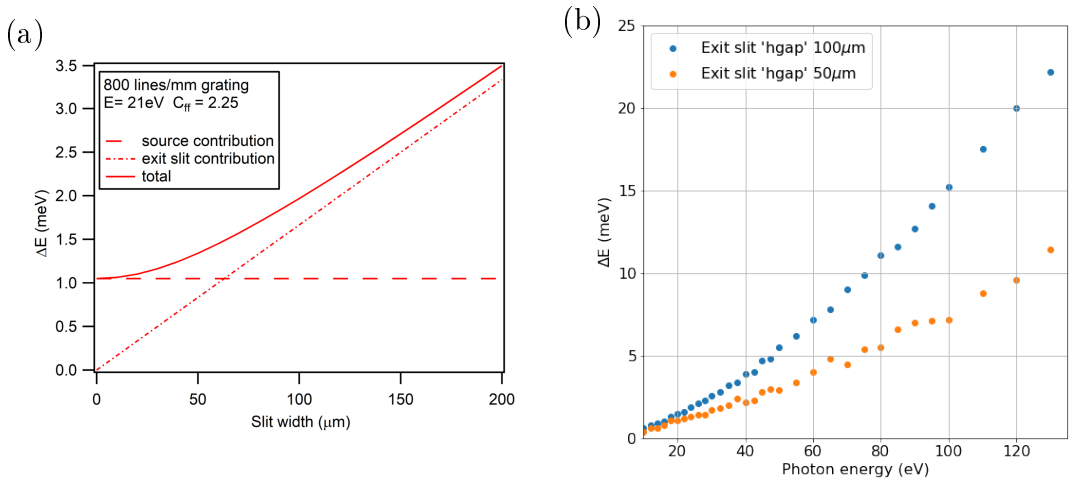

Figure 4.2: (a The slit width dependence of the energy resolution [102] and (b) the photon energy dependence based on ray-tracing for a 800 L/mm grating and a c_{ff} of 2.25 [100].

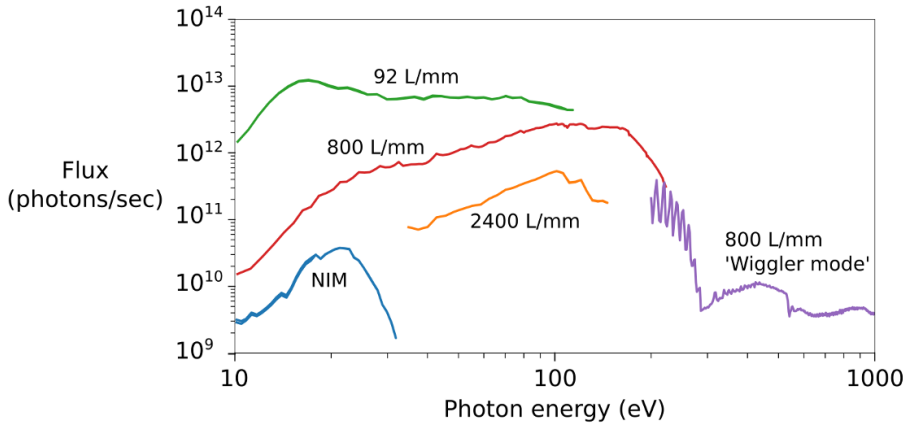

Figure 4.3: Overview of how the flux varies with photon energy for each grating mode. The image is taken from the Bloch beamline documentation [100].

enlarged by approximately 35 %. The refocusing method at Bloch relies on a single ellipsoidal mirror (M4) to directly image and demagnify the beam from the exit slit to the sample position. Consequently, the sample position should remain stationary when changing photon energy. It's important to note that with a $100 \times 100\,\mu m$ exit slit, a spot size of $10 \times 10\,\mu m$ is achieved at the sample position with 10:1 demagnification. However, using a $50 \times 50\,\mu m$ exit slit does not result in a spot size of $5 \times 5\,\mu m$ due to limitations imposed by slope errors in the M4 mirror. Nonetheless, this design ensures stable and reproducible sample positioning across the entire energy range.

4.3 Bloch end station

The Bloch beamline is split into two branches, the A-branch, dedicated to general ARPES, and the B-branch, specialized for spin ARPES applications. The research conducted for this thesis was exclusively carried out on the A-branch, thus the following discussion will focus on this branch. The A-branch consists of a series of ultra-high vacuum (UHV) chambers, including a load-lock, storage, scanning tunneling microscopy (STM), analysis chamber, two preparation chambers, and a radial distribution chamber that interconnects all chambers (see Figure 4.4) [100, 101].

Analysis chamber The experimental setup at the A-branch beamline includes an analysis chamber capable of maintaining a low base pressure in the upper 10^{-11} mbar range. With a double μ-metal liner, it ensures a residual magnetic field within the chamber of less than $0.1\,\mu T$ [101, 103]. The chamber is equipped with a DA30-L hemispherical analyzer from Scienta-Omicron and a 6-axis Carving cryomanipulator from Specs. The manipulator has a linear and angular precision of sub $1\,\mu m$ and 0.1°, respectively, and

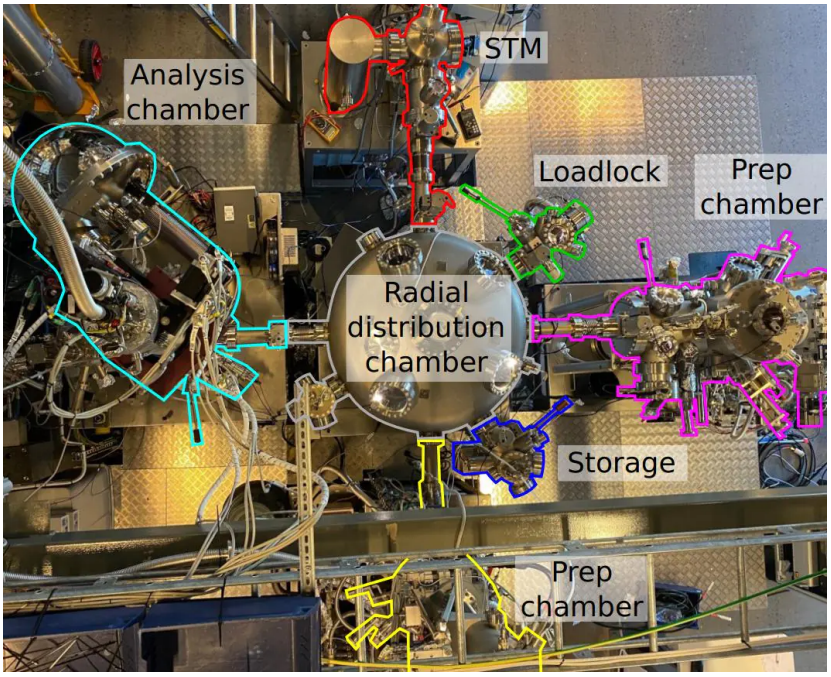

Figure 4.4: Overview of the A-branch endstation, highlighting all the UHV chambers. The photon beam enters from the left in this image. The image is taken from the Bloch beamline review [101].

can maintain a sample temperature range of 19 to 400 K during measurements. Additionally, the system allows for *in-situ* cleaving of top-posted single crystal samples and alkali metal (Rb, K, Cs) deposition, although simultaneous deposition during measurements is not supported. The ultimate energy resolution of 1.8 meV is not practically achievable due to a combination of residual grounding issues and the necessity to use higher pass energies ($5 - 20$ eV) at the kinetic energies typically employed. However, total energy resolution better than 10 meV is routinely achieved and can be pushed below 5 meV when needed.

Sample preparation chambers The end station is equipped with two preparation chambers operating within the low 10^{-10} mbar range, designed for sample treatment and growth. These chambers offer access to a sputter gun, LEED, and various heating options such as resistive heating (up to 900 °C), electron beam heating (up to 1400 °C), and direct current heating (up to 1200 °C) [101, 104]. Additionally, a new and specialized electron beam heating system was installed in one chamber, designed to reach temperatures as high as 2000 °C, as shown in Figure 4.5a, specifically added for the research conducted in this thesis. To facilitate silicon deposition for the research purposes of this thesis, a silicon wafer was also integrated into one of the preparation chambers, shown in Figure 4.5b. Furthermore, the chamber includes a port for introducing gases such as ethylene, which is used in this research. Cryogenic sample cooling is available for temperature control, with the capability to reach temperatures as low as 80 K using liquid nitrogen cooling and 40 to 50 K using liquid helium. The chambers are equipped with 4-axis manipulators, thickness monitors, and free ports with valves for mounting sources without venting. These features allow for a personalized sample preparation.

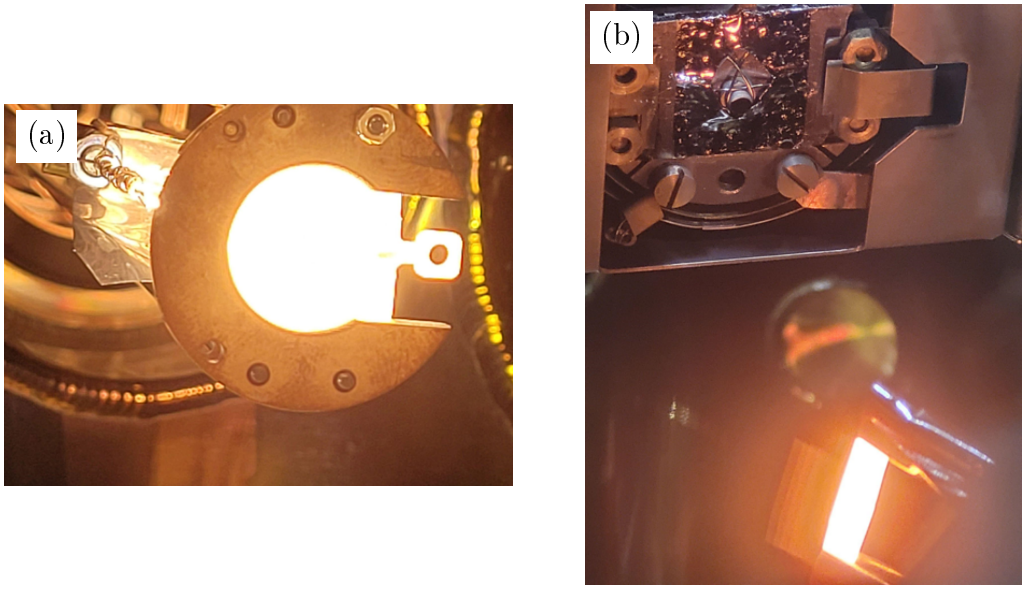

Figure 4.5: (a) Electron beam heating system that has heated the sample to about 2000 °C and (b) a silicon wafer heated up to emit and deposit silicon on the sample.

Chapter 5

Sample preparation

The TaC(111) crystal utilized in this study was provided by Princeton Scientific, with a miscut angle of 0.1°. The crystal was prepared in a hat shape with a polished surface of 2 mm in diameter, a base measuring 3 mm, and a height of 2 mm. To securely position the sample tantalum wires were wrapped around it and spot-welded to the sample holder at the beamline. Bartynski et al. [105] found a treatment of the TaC(111) surface involving a 10-minute sputter followed by repeated flashes to 2000 °C, that resulted in a well-ordered and stoichiometric surface region.

Initial investigations focused on identifying and removing any surface contaminants. Starting with a low temperature (c.a. 1000 °C) anneal, an XPS spectrum, called a survey spectrum, shown in Figure 5.1, provides an overview of the elemental composition of the sample and aids in the identification of surface contaminants. The survey spectrum suggests that all major contaminants have been removed by the annealing except for oxygen (the presence of hydrogen can not be directly determined since it lacks core electrons). The O 1s core level peak shows the presence of a surface oxide.

To remove the surface oxide, the sample was annealed several times, reaching temperatures up to 2000 °C. Figure 5.2 shows the change in the Ta 4f and O 1s core levels before and after this high-temperature anneal. This clearly shows the successful oxide removal, as the O 1s core level has almost vanished. For the subsequent measurements presented in the thesis, the O 1s core level reduced even further and often could not be distinguished from the background signal.

The Ta 4f core level has two spin-orbit split components: Ta $4f_{7/2}$ at lower binding

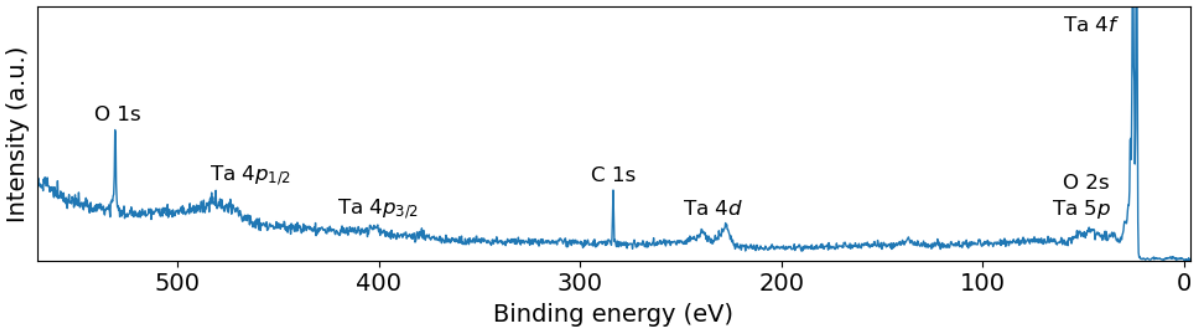

Figure 5.1: Survey spectrum ($h\nu = 650\,\text{eV}$) of the TaC(111) sample surface after annealing to 2000 °C, providing an overview of its elemental composition. The presence of the O 1s peak shows the existence of surface oxide.

energies, and Ta $4f_{5/2}$ at higher binding energies, further discussed in the main results. After a 2000 °C anneal, two components vanish; a large peak just above 24 eV and a smaller "shoulder" peak just below 23 eV, with the former peak being identified as the oxide peak. The latter peak will be discussed shortly and the other peaks will be examined in the next chapter.

LEED patterns, shown in Figure 5.3, demonstrate hexagonal symmetry of the TaC(111) surface, both before and after the oxide removal. However, the transformation from a 4×4 pattern to a clear 1×1 symmetry following oxide removal shows that a clean TaC(111) surface has been restored.

Further characterization using spatial maps of the band structure and Ta 4f core level revealed localized surface states, shown in Figure 5.4. The spatial maps show the region of interest (ROI) relative to a selected background region. In certain areas of the surface, unique band structures are found that match exactly the surface areas where the lower

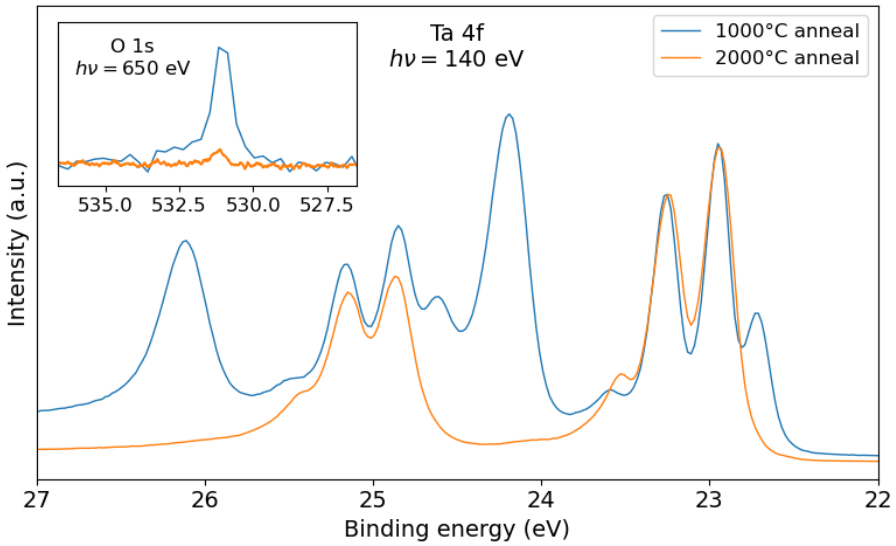

Figure 5.2: Ta 4f ($h\nu = 140$ eV) and O 1s ($h\nu = 650$ eV) spectra shown after annealing the sample to 1000 °C (blue) and then 2000 °C (orange), removing the surface oxide.

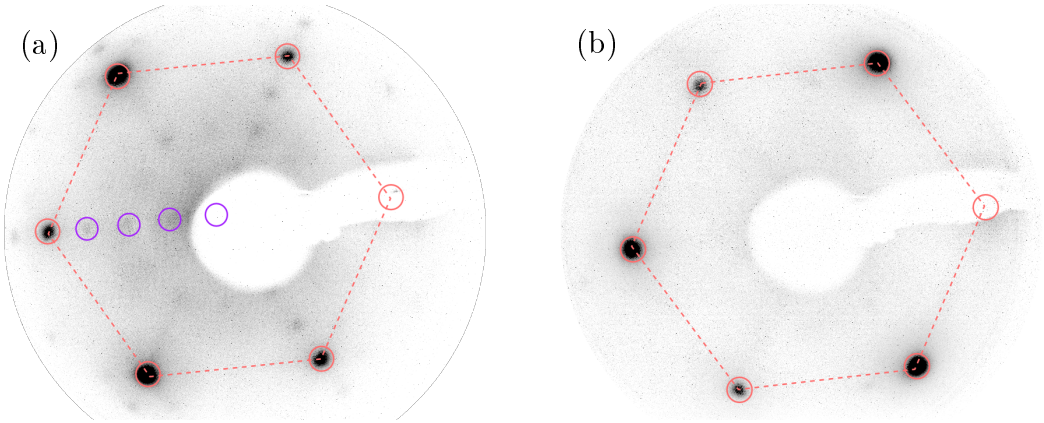

Figure 5.3: LEED images of the TaC(111) surface before (a) and after (b) removing the oxide layer. The 1×1 pattern in red shows the hexagonal structure of the sample. The purple circles indicate the 4×4 reconstruction of the surface oxide. The images were taken with an energy of 82 and 63 eV, respectively.

binding energy shoulder peak, observed in the Ta 4f spectrum (Fig. 5.2), is present. Other peaks in the Ta 4f core level are found to be uniform across the surface.

ARPES measurements of these surface bands show them along the $\overline{M}-\overline{\Gamma}-\overline{K}$ path (Fig. 5.4e. A photon energy scan (Fig. 5.4f) demonstrates the two-dimensional nature of these bands since they are constant with photon energy. These surface states seem not to have been previously reported in the literature, leading us to believe that they do not represent the expected clean Ta-terminated surface. Currently, the structural origin of this surface feature is unclear. Plausible origins include that these are either carbon-terminated or carbon-deficient surface regions. In subsequent sample preparations, these surface states became less frequently observed, leading us to not pursue further investigation of it.

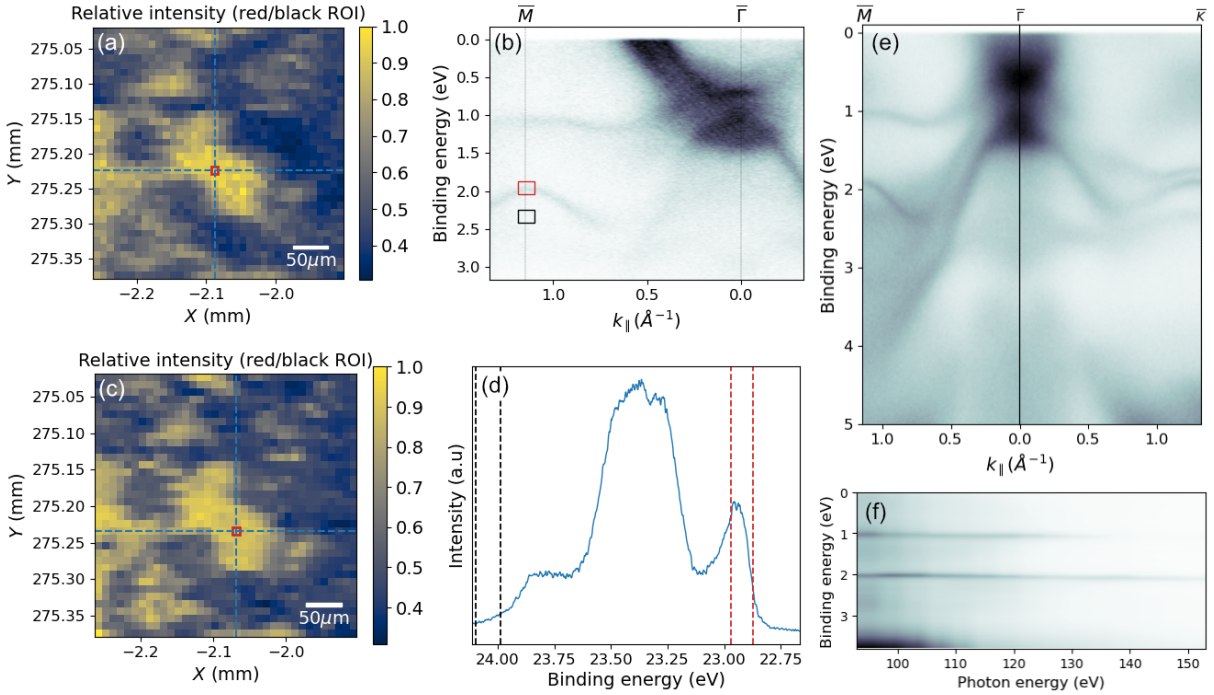

Figure 5.4: (a) Surface spatial map showing the contrast between the surface valence bands ($h\nu = 60\,\text{eV}$) and the background in (b). (c) Surface spatial map showing the contrast between the rightmost peak of the Ta 4f core level ($h\nu = 140\,\text{eV}$) and the background in (d). (e) Measured band structure in the $\overline{\Gamma}-\overline{M}$ and $\overline{\Gamma}-\overline{K}$ directions ($h\nu = 58\,\text{eV}$). The valence and core level spectra were measured at $h\nu = 60$ and $140\,\text{eV}$, respectively. (f) $h\nu$ resolved cut at $\overline{M}$ ($h\nu = 95-151\,\text{eV}$).

Chapter 6

Results

6.1 Clean TaC

After achieving a good sample surface, the investigation is shifted towards understanding the measured Ta 4f core levels. A fit of the measured spectrum is depicted in Figure 6.1a for a photon energy of 100 eV. The energy resolution of the fitted spectra presented in this thesis ranges from 10 to 44 meV. The observed spin-orbit split doublets revealed a 1.91 ± 0.01 eV separation between the lower energy Ta $4f_{7/2}$ and higher energy Ta $4f_{5/2}$ components. This finding aligns with prior studies, which found the separation to be within the range of $1.91 - 1.95$ eV [45, 105]. The reason for the increased width of the $4f_{5/2}$ components could be caused by additional decay channels of the de-excitation processes that lead to a broadening of its Lorentzian contribution. This broadening has been observed for the 4f core level in other period VI metals due to so-called Coster-Kronig processes [106].

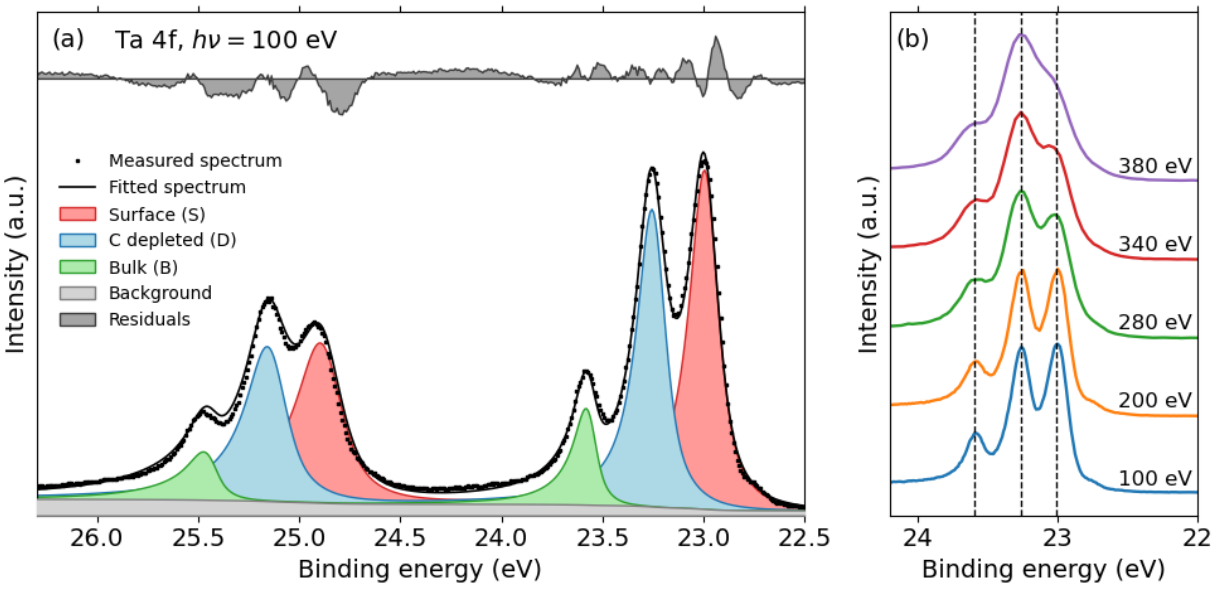

Figure 6.1: (a) Ta 4f core level fit at measured at $h\nu = 100$ eV along with the residuals (not to scale) between the fitted spectrum and the measured intensity. (b) Spectra of the Ta $4f_{7/2}$ core level at various photon energies. The spectra have been normalized to the most intense, central peak.

The primary Ta $4f_{7/2}$ peaks, denoted as S, D, and B, were measured at binding energies of 22.99 ± 0.05 eV, 23.26 ± 0.03 eV, and 23.59 ± 0.03 eV, respectively. The binding energy axis was calibrated by measuring the Fermi level and setting it as zero. Analysis of the fit yielded a Gaussian-Lorentzian ratio of 0.9 and a full width at half maximum (FWHM) of approximately 190 meV for these peaks. Previous investigations have reported surface and bulk peak positions within the ranges of $22.75 - 22.90$ eV and $23.35 - 23.56$ eV, respectively, with a separation of $0.56 - 0.60$ eV [5, 45, 105, 107]. Notably, these studies have consistently identified only two peaks. The reported bulk-surface separation suggests that the B and S peaks (green and red, respectively) in Figure 6.1a correspond to the bulk and surface peaks, as they fit this separation. This leaves the origin of the central peak, labeled D (blue), uncertain for now.

To validate the identification of the B and S peaks, the Ta 4f core level was measured at increasing photon energies, as illustrated in Figure 6.1b, focusing on the Ta $4f_{7/2}$ component. With increasing photon energy from 100 eV, the electron inelastic mean free path increases, resulting in a greater contribution of electrons originating from subsurface layers, namely the bulk [108]. Figure 6.2 depicts the change in the area of the S peak relative to the B and D peaks with increasing photon energy. Generally, the S peak diminishes relative to the other peaks, agreeing with its previous assignment as a surface component. This reasoning also identifies both the B and D peaks as bulk components.

A previous study has found evidence that the TaC(111) surface is stabilized through a charge redistribution around the surface, screening the long-range electric field created by the polar structure [45]. It suggests that the electron density at the first Ta layer increases, which enhances the screening of the positively charged cores of the surface atoms. This leads to a reduction in the Ta 4f binding energy, explaining the positioning of the red surface (S) component in Figure 6.1a. Furthermore, prior research has found that in the bulk, there is a charge transfer from Ta to C atoms so that the Ta 4f core level is at a higher binding energy than for a pure tantalum crystal [33, 34]. This charge transfer reduces with carbon concentration, leading to a reduction in binding energy. This hints at the blue bulk (D) component corresponding to a substoichiometric Ta site, while the green bulk (B) component corresponds to the stoichiometric Ta site. This possibility will be explored in the subsequent section.

Figure 6.3a shows ARPES measurements of the TaC(111) band structure at $h\nu = 56$ eV, tracing the surface Brillouin zone along the $\overline{\Gamma} - \overline{M}$ and $\overline{\Gamma} - \overline{K} - \overline{M}$ symmetry directions. All the following ARPES measurements are taken with a horizontal polarization of the light and have an energy resolution from 20 to 50 meV. The size of the Brillouin zone precisely matches a surface lattice constant of 3.15 Å, consistent with previous stud-

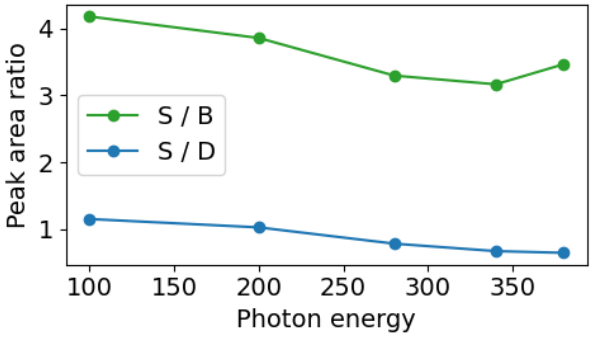

Figure 6.2: Changes in the area of the S peak relative to the B and D peak of the Ta 4f core level as photon energy is varied.

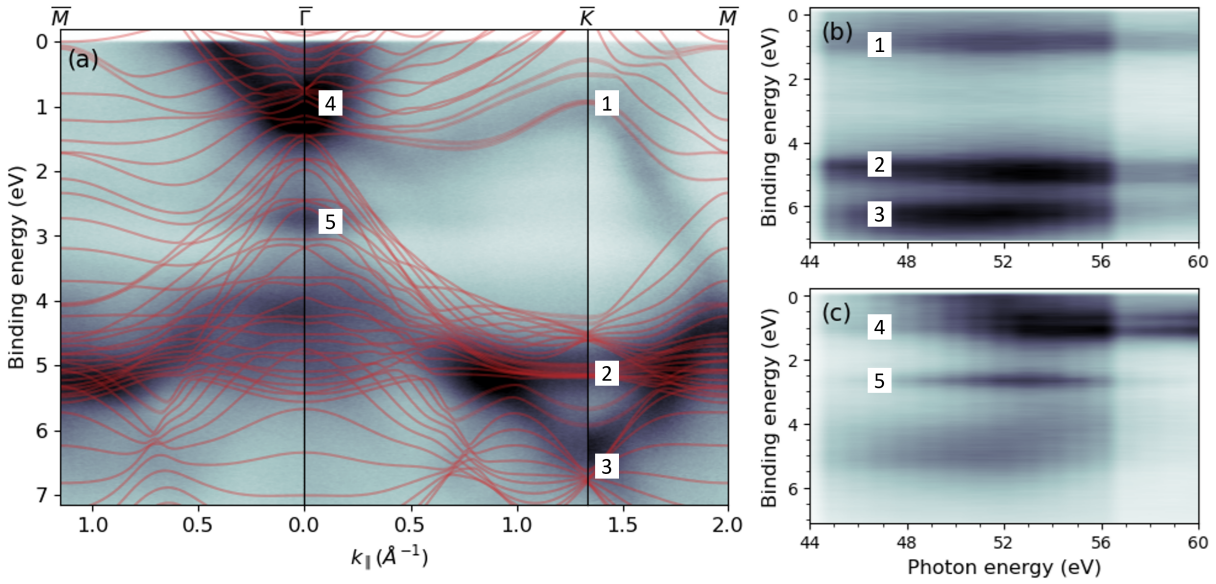

Figure 6.3: (a) TaC band structure ($h\nu = 56\,\text{eV}$) measured along the $\overline{\Gamma} - \overline{M}$ and $\overline{\Gamma} - \overline{K} - \overline{M}$ symmetry direction of the surface Brillouin zone. Overlaid is the DFT band structure calculation of a 31-layer Ta terminated TaC(111) slab. Photon energy scans at (b) $\overline{K}$ and (c) $\overline{\Gamma}$ show that the bands are surface induced, as they are constant with photon energy. The surface-induced bands are labeled 1 through 5.

ies [109]. Additionally, Figures 6.3b and c shows photon energy scans performed at $\overline{K}$ and $\overline{\Gamma}$, respectively. Changing the photon energy essentially changes the perpendicular component of the momentum space, which is related to the measured binding energy. Since surface states, by nature, do not have a perpendicular component, they do not vary with photon energy. Since the photon energy scans reveal bands that are constant with photon energy, the bands must originate from surface-induced states. Anazawa et al. identified four surface-induced bands within 2 eV of the Fermi level, derived from the Ta 5d orbitals [45]. However, only two of these bands are discernible in Figure 6.3a: band 1 around $\overline{K}$, descending in both the $\overline{\Gamma}$ and $\overline{M}$ directions, and band 4 centered around $\overline{\Gamma}$, extending to the Fermi level. Moreover, we observe two new surface states at $\overline{K}$, bands 2 and 3, at deeper binding energies, along with band 5, a flat band at $\overline{M}$ at a binding energy of approximately 2.5 eV, which may be related to defects. Overlaid in Figure 6.3a is a density functional theory (DFT) calculation of a 31-layer Ta terminated TaC(111) slab, done by Polley et al. [5]. The calculation predicts two spin-split states close to the Fermi-level at $\overline{K}$. Only one of these bands (band 1) is observed in the measurements, although it is not spin-split. Additionally, this band deviates from the calculations as it moves further from the $\overline{K}$-point, especially in the $\overline{M}$-direction. This discrepancy could be an indication that the TaC crystal does not have a perfect stoichiometry as the calculations assume.

At this point, various attempts were made at forming a SiC monolayer by depositing Si and annealing, all of which were unsuccessful. A possible explanation for this is that the TaC crystal lacks carbon so there is no carbon diffusion to the surface and bonding with Si. The higher intensity of the D peak compared to the B peak in the Ta 4f core level (Fig. 6.1a) might be an indication of this if the theory that they correspond to different local carbon compositions proves true. To test this the effects of carbon deposition are examined.

6.2 Carbon deposition and TaC stoichiometry

Building upon our study of the TaC(111) surface, I now focus on carbon deposition. Although TaC is stable in a broad range of carbon concentrations, prior investigations of the TaC(111) core levels often suggest a fully stoichiometric or nearly stoichiometric surface region [5, 45, 105]. None of these studies have reported the presence of the central Ta 4f component (D peak) observed in the measurements presented here. This discrepancy motivates us to investigate whether this additional peak is related to carbon deficiency.

To address this question, the sample was subjected to successive carbon depositions via ethylene (C_2H_4) exposure. Heating the sample to approximately 950 °C induced the TaC(111) surface to act as a catalyst, enabling the cracking of ethylene molecules that results in the deposition of atomic carbon. The exposure, or dosage, is quantified in langmuir (L), calculated by multiplying the gas pressure by the exposure time. One langmuir is defined as an exposure of 10^{-6} Torr for one second, or equivalently 10^{-8} Torr for 100 seconds.

Figure 6.4 illustrates the evolution of the C 1s and Ta $4f_{7/2}$ core levels with increasing ethylene exposures. The two bulk components of the Ta $4f_{7/2}$ core levels retained binding energies consistent with previous measurements. However, the surface component showed fluctuation in the range of 22.92 − 23.02 eV, indicating that surface modifications occur during the exposure process.

The carbon 1s core level is known to have two components that correspond to the bulk and surface environments. The core level of the C 1s spectra after a 10 L ethylene exposure

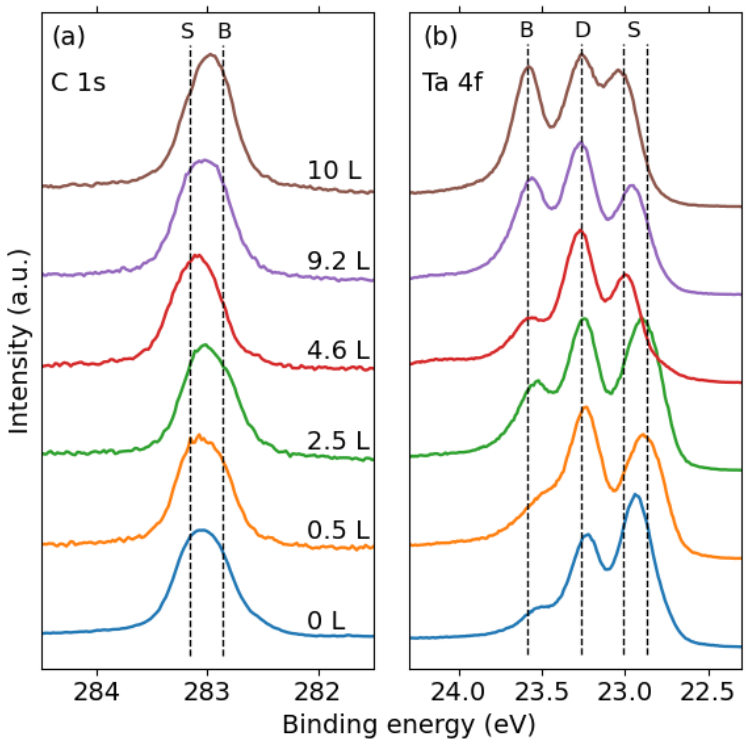

Figure 6.4: (a) C 1s ($h\nu$ = 430 eV) and (b) Ta 4f ($h\nu$ = 140 eV) core levels at increasing ethylene exposures. The S, B, and D labels represent the surface, stoichiometric bulk, and substoichiometric bulk environments of the TaC(111) crystal, respectively. The spectra are normalized to their highest feature.

was therefore fitted with two peaks, which is shown in Figure 6.5a. The fitting procedure then estimates the widths of these peaks. The residuals in the fit have relatively small variations across the whole spectrum indicating that there are no other major carbon environments. From the fit, the two peaks were found to have a binding energy of 282.86 and 283.13 ± 0.06 eV. These binding energies align closely with those reported by Polley et al., who attributed them to bulk and surface components, respectively [5]. Across the various ethylene exposures, there is negligible change in the binding energy of either peak.

Regarding the Ta 4f bulk peaks, if the hypothesis where one corresponds to a stoichiometric region and the other to a carbon-depleted region is correct, I anticipate that their intensities will vary inversely since they represent opposing atomic environments. Figure 6.5b illustrates the changes in the area of the Ta 4f B peak relative to the D peak with increasing total ethylene exposure. The graph's different colors indicate separate sample preparations, which were conducted to remove deposited silicon forming SiC, as discussed in the subsequent section. Additionally, it should be noted that all ethylene exposures were conducted at a pressure of 1×10^{-8} mbar except for the 10 L exposure, which was performed at 1×10^{-7} mbar. In general, we observe a relative rise in the intensity of the B peak with increased ethylene exposure. Importantly, this trend is consistent within each sample preparation. The temporary drop observed between 2.5 and 4.6 L exposures may be due to initial variations in the C:Ta molar ratios induced by annealing during the sample preparation. Despite efforts to maintain consistency in sample preparation, some degree of variability is unavoidable. This variability extends to ethylene exposure and cracking efficiency, which are influenced by surface temperature and potentially the pressure at which ethylene is introduced. These factors could also account for the notable increase in the peak area ratio following the 10 L exposure. Overall, the observed growth of the B peak suggests an increasing prevalence of its corresponding chemical environment. This implies that the additional carbon diffuses into the sample, enhancing its stoichiometry. The next step is to deposit silicon with the aim of forming a SiC monolayer.

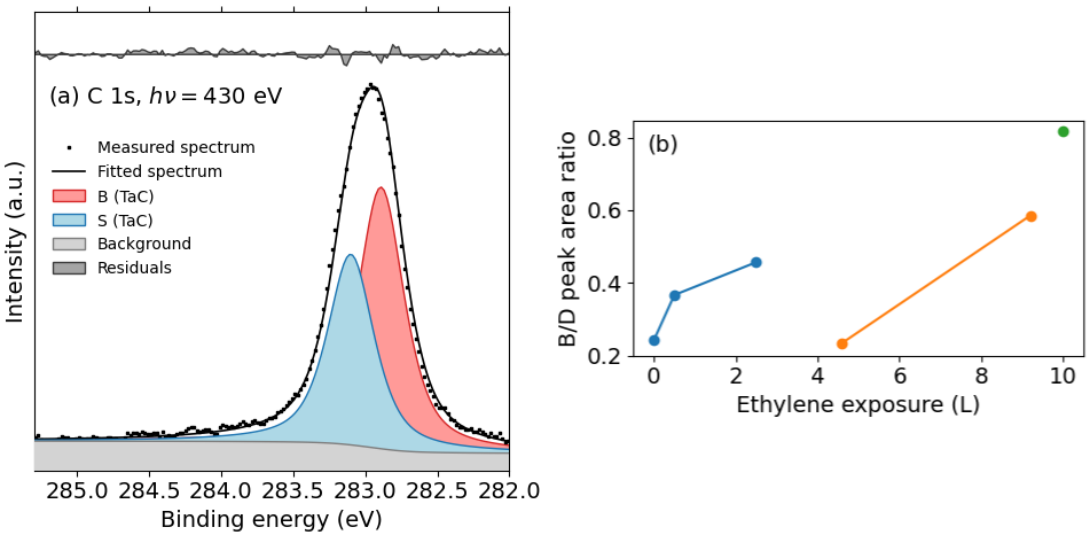

Figure 6.5: (a) C 1s core level fit of spectra measured after 10 L ethylene exposure at $h\nu = 430$ eV and 140 eV, respectively, along with the residuals (not to scale) between the fitted spectrum and the measured intensity. (b) The area ratio of the bulk (B) and carbon depleted (D) Ta 4f peaks with increased total ethylene exposure. The different colors indicate that the sample was annealed for a fresh sample preparation.

6.3 Silicon deposition and the formation of a honeycomb SiC monolayer

Following the 10 L carbon deposition, silicon was deposited onto the sample by heating a Si wafer with a 7 A current for 10 minutes. Si atoms thermally evaporate when the wafer gets hot enough, some of which deposit on the sample's surface. Subsequently, the sample was annealed at 920 °C for 3 minutes. The resulting LEED pattern, presented in Figure 6.6, shows a 1×1 surface structure similar to the clean TaC(111) surface. However, a comparison with the LEED pattern of the clean surface (Fig. 5.3b) reveals a reversal in spot intensities at the same beam energy, indicating the formation of a new surface structure.

Analysis of the core levels, as depicted in Figure 6.7, reveals notable changes. New peaks in the C 1s and Si 2p spectra emerge at binding energies of 282.38 ± 0.06 eV and 99.93 ± 0.03 eV (Si $2p_{3/2}$ component), respectively. These values closely align with the

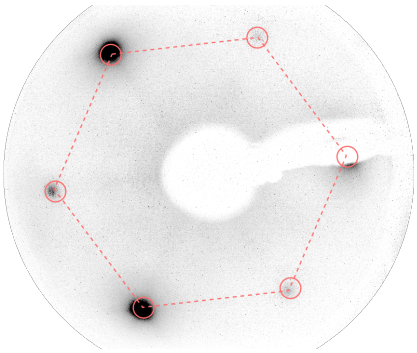

Figure 6.6: LEED image of a SiC monolayer on TaC(111) taken with a beam energy of 63 eV. The pattern reveals a 1×1 hexagonal structure of the sample, highlighted in red. The intensity of the peaks is reversed relative to the pattern obtained from the clean TaC sample, seen in Figure 5.3b at the same energy.

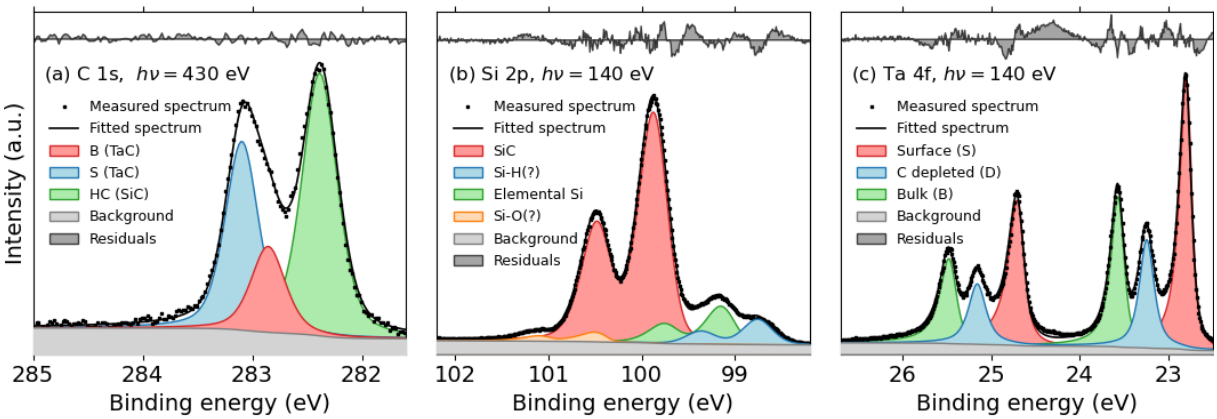

Figure 6.7: (a) C 1s ($h\nu = 430$ eV), (b) Si 2p ($h\nu = 140$ eV) and (c) Ta 4f ($h\nu = 140$ eV) core level fits of spectra measured after 10 L ethylene exposure and 10 min Si deposition, along with the residuals (not to scale) between the fitted spectrum and the measured intensity. The Si core level is split into the $2p_{3/2}$ and $2p_{1/2}$ spin-orbit components at a lower and higher binding energy, respectively. Similarly, the Ta core level is split into the $4f_{7/2}$ and $2p_{5/2}$ spin-orbit components at a lower and higher binding energy, respectively.

binding energies observed for a SiC monolayer by Polley et al. [5] at 282.48 and 100.04 eV, respectively. Note that the Si 2p core level shows two spin-orbit split components, with the Si $2p_{3/2}$ state at lower energies and the Si $2p_{1/2}$ state at higher energies. Additionally, the surface (S) peak of the Ta 4f core level shifts to 22.83 ± 0.03 eV, consistent with the value of 22.84 eV reported by Polley et al. The proposed sample structure, described in Figure 2.2c, explains the origin of these components (excluding the D peak).

In addition to the main Si 2p peak (red), three minor peaks are observed, the origins of which remain uncertain. However, elemental Si typically has a $2p_{3/2}$ binding energy of approximately 99.2 eV [110], closely matching the green component at 99.16 ± 0.03 eV. The blue lower binding energy peak could correspond to hydrogen-bonded silicon species (Si monohydride or dihydride), potentially introduced during ethylene exposure [111, 112]. Because we cannot verify that there are no trace amounts of oxygen, the remaining higher binding energy peak in orange may belong to an oxide state. Nevertheless, the presence of these residual peaks suggests that more Si was deposited onto the surface than is required for SiC monolayer formation.

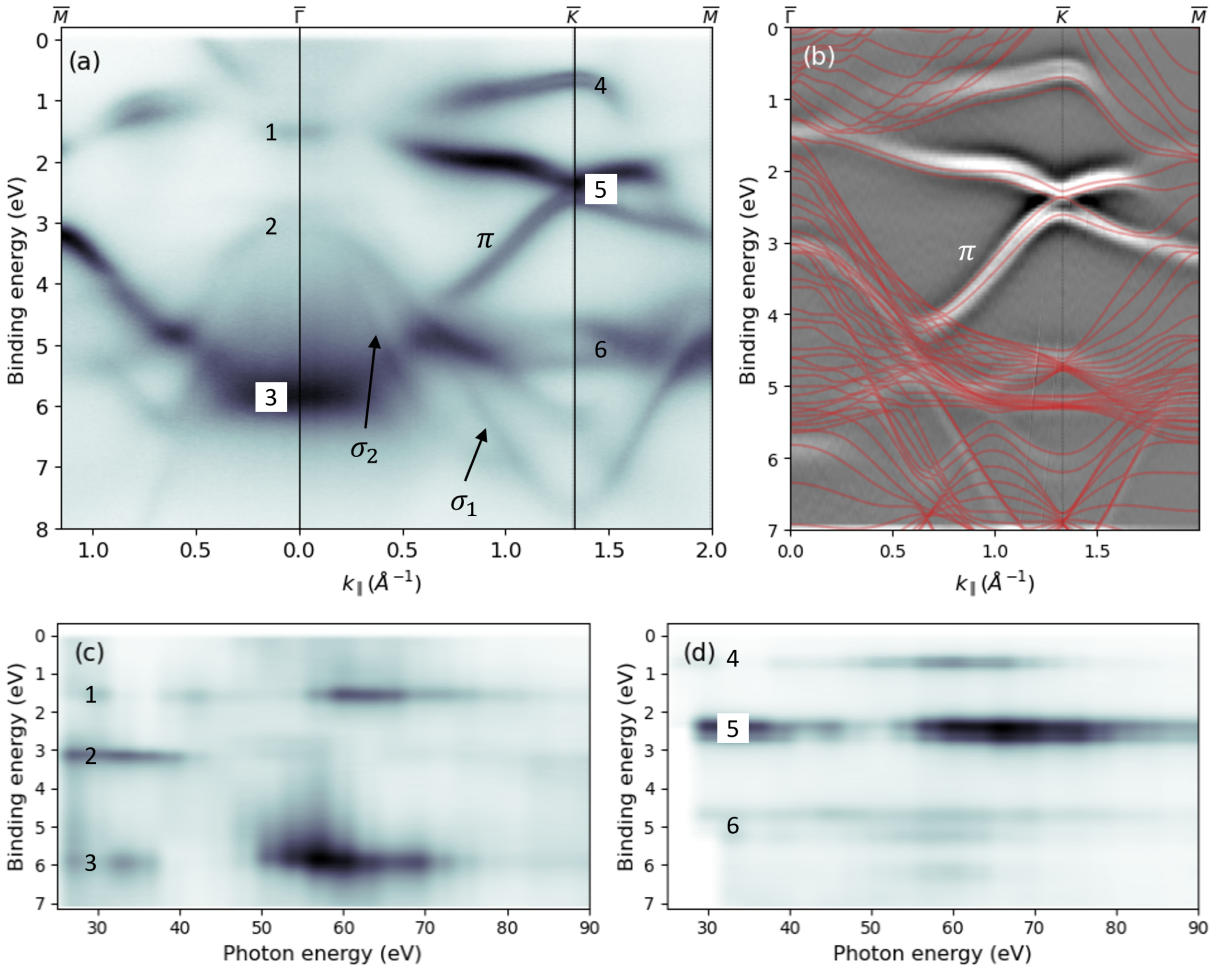

Figure 6.8: (a) Measured band structure of a SiC monolayer on TaC(111) at $h\nu = 56$ eV. (b) High-resolution measurement, presented as a second derivative image, highlights the band structure around $\overline{K}$, obtained by integrating many spectra measured over $h\nu = 24$ to 90 eV. A DFT calculated band structure (red) has been superimposed on the measured bands and shifted down by 200 meV to align better with the $\overline{K}$-point crossing at 2.35 eV binding energy. Photon energy scans at (c) $\overline{\Gamma}$ and (d) $\overline{K}$ with the labeled surface induced bands.

The synthesis of a honeycomb SiC monolayer is strongly supported by ARPES measurements of the electronic band structure. These bands are depicted along the $\overline{\Gamma} - \overline{M}$ and $\overline{\Gamma} - \overline{K} - \overline{M}$ symmetry directions of the surface Brillouin zone in Figure 6.8a. Photon energy scans (Figs. 6.8c and d) reveal a two-dimensional nature of these states. Remarkably, the observed band structure perfectly matches that measured by Polley et al. [5], providing conclusive evidence for the formation of a SiC monolayer atop the TaC(111) surface.

In Figure 6.8b, a DFT calculation of the SiC band structure atop the TaC(111) substrate (done by C. Polley, a colleague at the Bloch beamline) is superimposed on a high-resolution second derivative image of the band structure around $\overline{K}$. This comparison reveals excellent agreement between calculations and measurements. However, to achieve better alignment with the $\overline{K}$-point crossing at 2.35 eV, the calculated band structure has been shifted down by 200 meV, resulting in slight misalignment of the upper bands. Although the origin of this discrepancy is unknown, my best judgment is that it may be resolved by using more sophisticated computational techniques.

Surface-induced bands around $\overline{K}$ display clear spin-orbit splitting, with approximately 230 and 240 meV splitting observed for the upper band and the lower set, respectively. This phenomenon is supported by band structure calculations that consider the interaction with the TaC substrate (see Fig. 2.3b). These calculations demonstrate that the interaction induces hybridization of the π bands of the SiC layer with TaC surface states, leading to pronounced spin-orbit splitting and a Dirac-like crossing at $\overline{K}$ approximately 2.35 eV below the Fermi level [5]. The fact that these calculations account for essentially all observations in the measured band structure gives unambiguous confirmation of the 2D SiC synthesis. This result allows us the opportunity to explore the limits of the growth process and see how flexible the growth conditions can be.

6.4 Growth process and graphene formation

In this section, I aim to discover how adjustable the parameters of the growth process are by observing step-by-step the deposition of an excess amount of carbon and silicon. The preparation steps for this growth procedure are summarized in Table 6.1. Beginning with a clean TaC(111) surface, the sample undergoes exposure to ethylene in three incremental steps, each at a significantly higher dose than the previous. Subsequently, silicon is deposited onto the surface in two increments. During the initial Si deposition, the sample is examined both before and after annealing the surface to enable Si atom structuring.

Figure 6.9 illustrates the evolution of C 1s, Si 2p, and Ta $4f_{7/2}$ core levels throughout each preparation step. The initial clean TaC(111) sample has spectra similar to those measured in section 6.1. Following the 12 L ethylene exposure, the Ta 4f bulk (B) peak grows significantly at the expense of the D peak (Fig. 6.10b). This suggests that carbon-depleted sites are being refilled which increases the amount of Ta atoms that experience a local stoichiometric environment. Since there is a fixed amount of Ta atoms, this must lead to a reduction in the substoichiometric Ta environment and a less intense D peak. Simultaneously, the intensity of the C 1s peak shifts to the bulk (B) component, which is to be expected since the carbon amount in the bulk is increasing with the C deposition.

A new peak is also observed at 285.15 ± 0.06 eV which grows significantly after an additional 15 L ethylene exposure, bringing the cumulative dose to 27 L. This peak is attributed to graphene since it aligns well with previous studies of monolayer graphene on TaC(111) which report its position at approximately 285.1 eV [109,113]. Furthermore,

Table 6.1: Sample preparation steps showing how much ethylene was exposed to the surface and the silicon deposition time. The numbers represent a cumulative amount. Ethylene exposure occurred at a pressure of 10^{-7} mbar and Si depositions occurred at 7 A wafer current.

Prep. step	Ethylene exposure (L)	Si dep. (min)	Notes
1	0	0	Clean surface, several high temperature anneals up to 2000 °C
2	12	0	Sample at 950 °C during ethylene exposure
3	27	0	Sample at 950 °C during ethylene exposure
4	57	0	Sample at 950 °C during ethylene exposure
5	57	2.5	Room temperature Si deposition
6	57	2.5	Sample annealed for 4 min at 950 °C
7	57	5.0	950 °C substrate temperature during Si deposition

the Ta 4f surface peak has shifted by about 90 meV, relative to the clean TaC(111), to a higher binding energy of 23.08 ± 0.03 meV. This shift is likely induced by the new graphene environment experienced by the Ta surface atoms. Through core level fitting, the peak's width was observed to increase in preparation step 2 which is indicative of more than one Ta environment. This suggests that the graphene coverage is incomplete and there are still surface Ta atoms exposed to the vacuum. In the next step, as the graphene peak grew, the Ta surface peak returned to the previous width. This means that they all share the same environment, indicating complete graphene coverage.

The fit of core levels at this preparation step is depicted in Figure 6.10a. The graphene peak is labeled C=C for its sp^2 bonds. The FWHM of this peak is approximately 700 meV, compared to about 400 meV for the B and S C 1s peaks. This type of widening occurs when there are some variations in the atomic environment, potentially indicating that the graphene is interacting with the substrate. This phenomenon has been identified as the main factor leading to the broadening of the C 1s core level in graphene atop various metals [114]. The reason for the broadening was a strong interaction between the graphene and the underlying substrate, leading to strain-induced corrugation of the graphene and thus carbon that sit at different distances to the substrate.

The core level fit (Fig. 6.10a) reveals the presence of two additional peaks at either side of the main graphene peak. While their origins have not been experimentally verified, comparisons to existing literature provide insights. The lower binding energy peak at 284.39 ± 0.06 eV is tentatively assigned to hydrogen-terminated graphene edge states or single bonded sp^3 carbon. This state, at lower binding energies relative to the main graphene peak, has been observed in hydrogen-terminated graphene nanoribbons on transition metal substrates [115, 116] and for C–C sp^3 bonds induced by defects [117, 118]. Additionally, its proximity to the binding energy of suspended few-layer graphene at

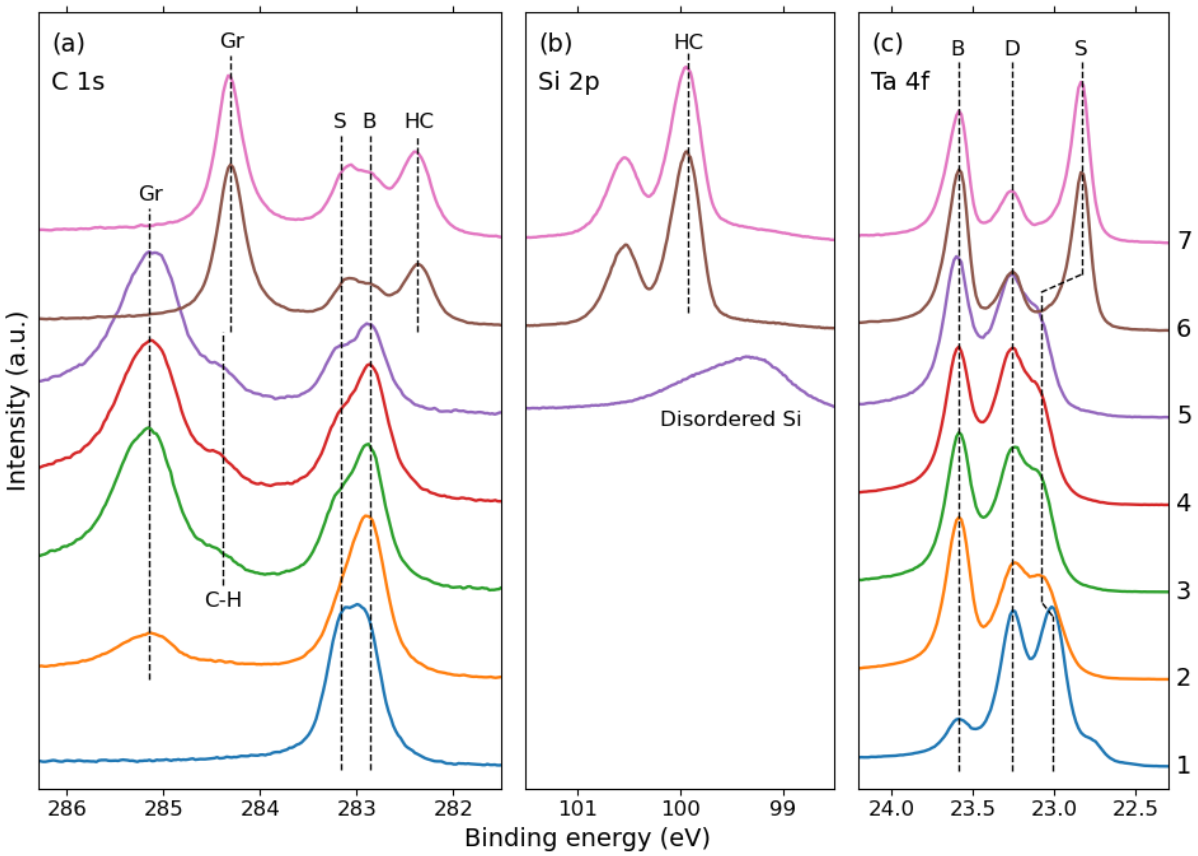

Figure 6.9: (a) C 1s ($h\nu$ = 430 eV), (b) Si 2p ($h\nu$ = 140 eV) and (c) Ta 4f ($h\nu$ = 140 eV) core level of spectra measured after different preparation steps, described in Table 6.1. The peaks are labeled according to their structural origin. Gr, HC, and C–H indicate graphene (C=C), honeycomb SiC, and carbon-hydrogen bonded environments, respectively, while S, B, and D represent the surface, stoichiometric bulk, and substoichiometric bulk environments of the TaC(111) crystal, respectively.

284.47 eV [119] suggests the possibility of originating from second-layer graphene, although the negligible ethylene cracking efficiency on the graphene surface makes this scenario unlikely. The higher binding energy peak at 285.64±0.30 eV exhibits a broader width compared to the other peaks, indicating an ill-defined carbon environment. This peak is provisionally assigned as adventitious carbon (AdC) or C-vacancy sites in the graphene. AdC is predominantly made of decoupled hydrocarbon (C–H) and sp^3 bonded carbon (C–C) on sample surfaces and has been observed in the range of 284.08 – 286.74 eV [120–123] Additionally, C-vacancy sites have been observed at higher binding energies relative to the main graphene peak [118, 124].

Figure 6.10b tracks the changes in the peak area of all Ta 4f components with each preparation step. Thus far, the total area of the Ta 4f core level spectrum has been decreasing (see Fig. 6.10b). Since there should be no change in the amount of Ta atoms, this decrease is attributed to a burying effect of the newly formed graphene. As the graphene covers the TaC surface, fewer electrons escape from the deeper Ta layers. However, following an additional 30 L exposure (over a doubling of the total dose) no significant changes are observed in the total area of the Ta 4f core levels, nor their shape (Fig. 6.9). This suggests that the surface had already been saturated with graphene coverage, showing that the graphene formation is self-limiting. Since the chemically active polar TaC(111)

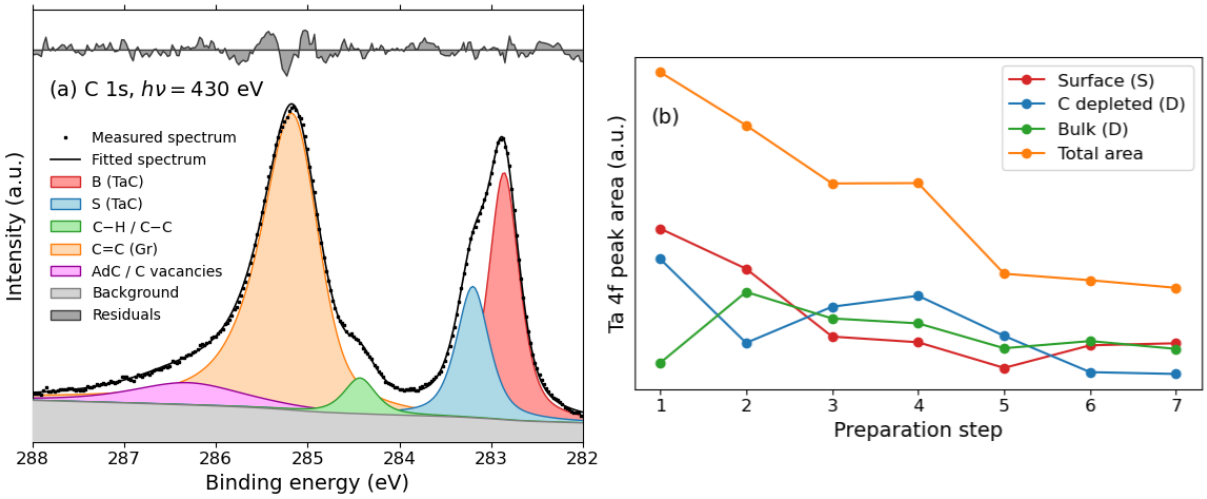

Figure 6.10: (a) C 1s ($h\nu = 430\,\text{eV}$) core level fit after a 27 L ethylene exposure (preparation step 3, as is described in Table 6.1), along with the residuals (not to scale) between the fitted spectrum and the measured intensity. The B and S labels represent the bulk and surface carbon environments in the TaC(111) crystal, respectively. The C–H, C–C, and C=C labels indicate carbon-hydrogen bands, and sp^3 and sp^2 carbon-carbon bonds, respectively, with the last corresponding to graphene. Lastly, AdC signifies adventitious carbon, discussed in the text, and C vacancies refers to vacancy defects in the graphene. (b) Peak area for all components in the Ta 4f core level for all the different sample preparations described in Table 6.1 (shown qualitatively in Figure 6.9c).

surface acts as a catalyst for cracking the ethylene into its atomic counterparts, when it gets fully blocked, ethylene does not crack (at least not nearly as efficiently) and carbon is no longer deposited.

Following silicon deposition at room temperature (preparation step 5 in Table 6.1), a feature in the Si 2p spectrum appears, seen in Figure 6.9b, characteristic of a disordered structure. This disordered silicon surface buries the underlying layers and thus decreases the intensity of the other core levels, which is demonstrated in the drop in total area of the Ta 4f core level, shown in Figure 6.10b. After a four-minute anneal at 950 °C, evidence of SiC monolayer formation emerges. This is indicated by the band structure measurements (discussed later) and the appearance of new C 1s (HC) and Si 2p (HC) peaks at the same binding energies as the SiC peaks observed previously in Section 6.3.

The other changes observed are the shift in the Ta 4f surface and graphene components to lower binding energies (see Fig. 6.9c). This suggests major changes in both environments upon SiC monolayer formation which is well explained if the SiC monolayer formed underneath the graphene. This could be expected considering the lattice matching between the SiC monolayer and the TaC surface, making it a more favorable substrate for growth. However, stronger evidence for this is the shift of the Ta 4f surface component to $22.83 \pm 0.03\,\text{eV}$ which matches with the binding energy of the same component in Section 6.3, where 2D SiC was formed on the TaC(111) surface. Moreover, the binding energy of the graphene peak shifted to $284.31 \pm 0.06\,\text{eV}$ upon SiC monolayer formation, approximately 100 meV lower than observed for single-layer graphene on a bulk 6H-SiC(0001) surface [125, 126]. Notably, this peak has an FWHM of about 300 meV, a reduction of 400 meV compared to the previous graphene peak. This narrowing of the width and shift to lower binding energies are similar to quasi free-standing graphene on iridium, where the C 1s core level is dominated by a single narrow component due to weak

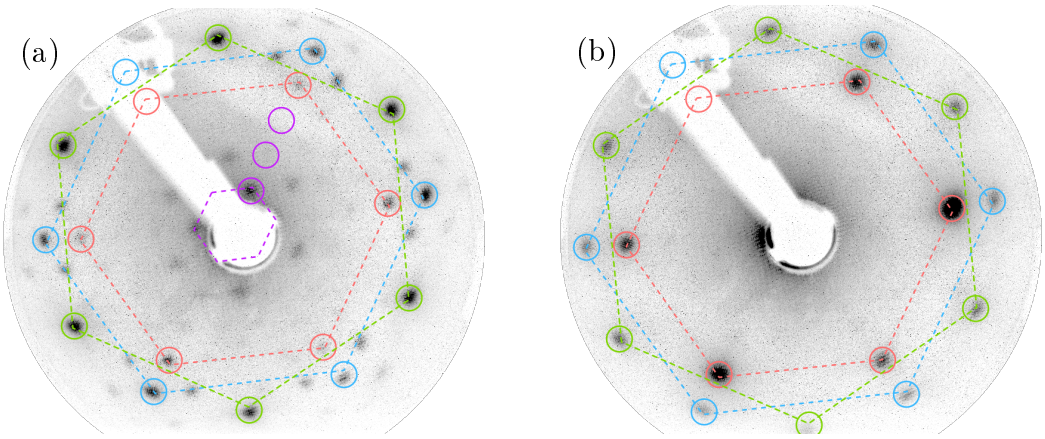

Figure 6.11: (a) LEED image of graphene on the TaC showing a 1×1 hexagonal structure of the TaC(111) surface (red), as well as two rotational graphene domains, one oriented along the TaC(111) surface (blue) and the other rotated by 30° (green). Additionally, there is a 4×4 coincidence structure resulting from lattice matching of the graphene and TaC(111) surface. (b) LEED image of a graphene after a SiC monolayer has formed underneath showing the same pattern as before, with the exception that the coincidence lattice has disappeared. Both LEED images are taken at a beam energy of 73 eV.

substrate interaction [114]. These observations suggest that graphene is interacting less with its environment, which is well explained if the SiC monolayer has intercalated at the TaC(111)-graphene interface, decoupling graphene from the TaC(111) surface. Finally, since the graphene layer remains at this step, carbon must have been extracted from the TaC crystal to form the SiC monolayer.

In the final preparation step, the amount of deposited silicon is doubled, yet minimal changes are observed in the Ta 4f peak areas and other core levels. This suggests that the surface has either reached or was near saturation with a SiC monolayer coverage. Like graphene, the formation of a SiC monolayer seems to be a self-limiting process. This is likely because the π orbitals of the SiC monolayer hybridize with the underlying TaC(111) surface states, leaving no free bonds for a second layer to form.

The LEED image of the sample at preparation step 3 (see Table 6.1) is shown in Figure 6.11a where graphene had formed on the TaC surface. In addition to the 1×1 structure of the TaC(111) surface (in red), the LEED pattern shows two new hexagonal 1×1 structures, corresponding to the two rotational graphene domains, in blue and green, respectively. One of the domains is aligned along the TaC(111) surface and the other is rotated by 30°. Moreover, a smaller hexagonal pattern (in purple) is suspected to be a coincidence lattice between the graphene and TaC surface. This would imply that the graphene is strained as it attempts to match the periodicity of the TaC surface, corroborating the core level observation that suggests the same. The coincidence structure seems to have a 4×4 lattice with respect to the TaC(111) surface, indicating that it repeats every four periods of TaC(111) unit cell and every five periods of graphene. With a TaC(111) surface lattice constant of 3.15 Å, this implies a coincidence lattice of 12.6 Å and an expanded graphene lattice of 2.52 Å, compared to 2.46 Å for non-strained graphene [127].

Figure 6.11b shows the LEED image of the sample at preparation step 6 (see Table 6.1) where 2D SiC had formed underneath the graphene. The same hexagonal patterns are seen for the SiC monolayer and graphene as previously. However, the coincidence lattice has now disappeared, showing that the graphene is incommensurate with the substrate

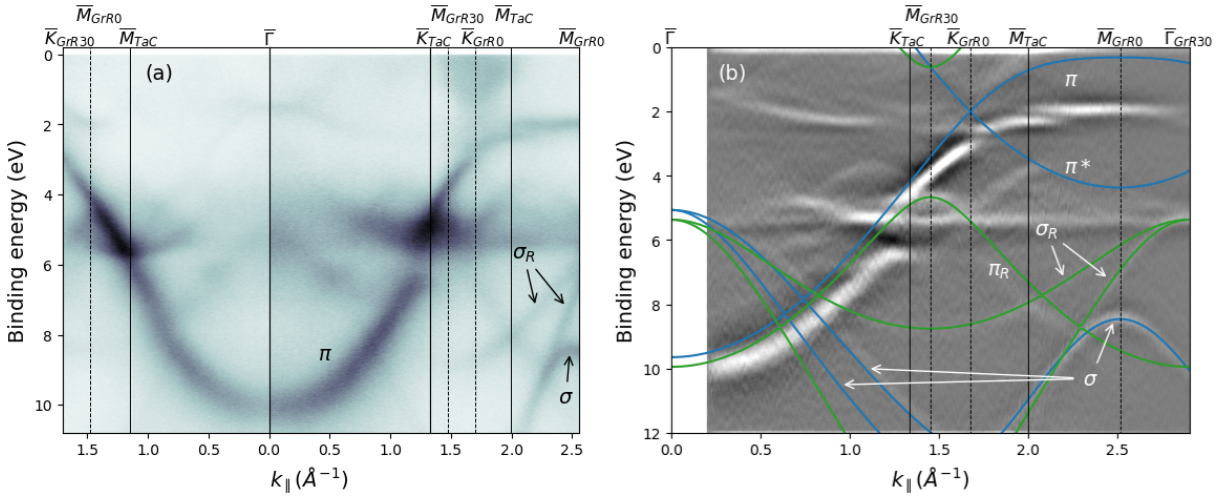

Figure 6.12: (a) Measured band structure of graphene on a TaC(111) ($h\nu = 100\,\text{eV}$). (b) Higher resolution measurement around the $\overline{K}$-point, obtained by integrating over $h\nu = 54 - 144\,\text{eV}$, with superimposed DFT calculated graphene bands. The graphene bands show two domains, one oriented the same way as the TaC surface (blue), and the other rotated by 30° (green). The calculated graphene bands are shifted down by 2.0 and 2.3 eV for the non-rotated and rotated domains, respectively, to align the σ bands with the measurement.

and is thus no longer strained. This agrees with previous core level measurements that suggest a weaker bonding between the graphene layer and its surroundings. Additionally, by aligning several symmetry points in the ARPES measurements and reconstructing the graphene Brillouin zone, the graphene was observed to change from a strained lattice constant of about 2.50±0.01 Å (consistent with prior studies [109,113]) to the non-strained constant of 2.46 ± 0.01 Å following the SiC monolayer formation.

ARPES band structure measurements of graphene on TaC(111) (preparation step 3 in Table 6.1) are shown in Figure 6.12a for both the $\overline{\Gamma} - \overline{M}$ and $\overline{\Gamma} - \overline{K}$ symmetry directions. By identifying the π and σ bands, the band structure reveals the presence of two rotational graphene domains, one rotated 30° from the other. To compare with theory, the DFT-calculated band structure (provided by C. Polley) of freestanding graphene is superimposed on a second derivative image of the measured bands in Figure b. Due to a strong interaction with the substrate, the calculated bands had to be shifted down by 2.0 and 2.3 eV to align the σ bands for the non-rotated and rotated graphene domains, respectively. The comparison between theory and measurement shows that the π band is significantly distorted, as it does not reach the Fermi-level. Previous studies have also observed this for the same system [109, 113]. This distortion, along with the vanishing of the Dirac-crossing indicates that the π band hybridizes with the TaC surface states, demonstrating the strong interaction between the graphene and the TaC substrate.

Figure 6.13a depicts the ARPES band structure measurements of graphene on 2D SiC (preparation step 6 in Table 6.1). Again, by identifying the π and σ bands, the two rotational domains of the graphene are observed. These measurements are accompanied by the DFT calculated band structure of freestanding graphene and SiC monolayer coupled to the TaC(111) substrate (provided by C. Polley), superimposed on the measured second derivative band structure in Figure b. This clearly distinguishes the origin of each band. Since the 2D SiC bands match the calculations, it supports the description that the SiC monolayer has indeed formed underneath the graphene. If it had formed on top, the band structure would have changed since it is highly sensitive to the sample structure. Note

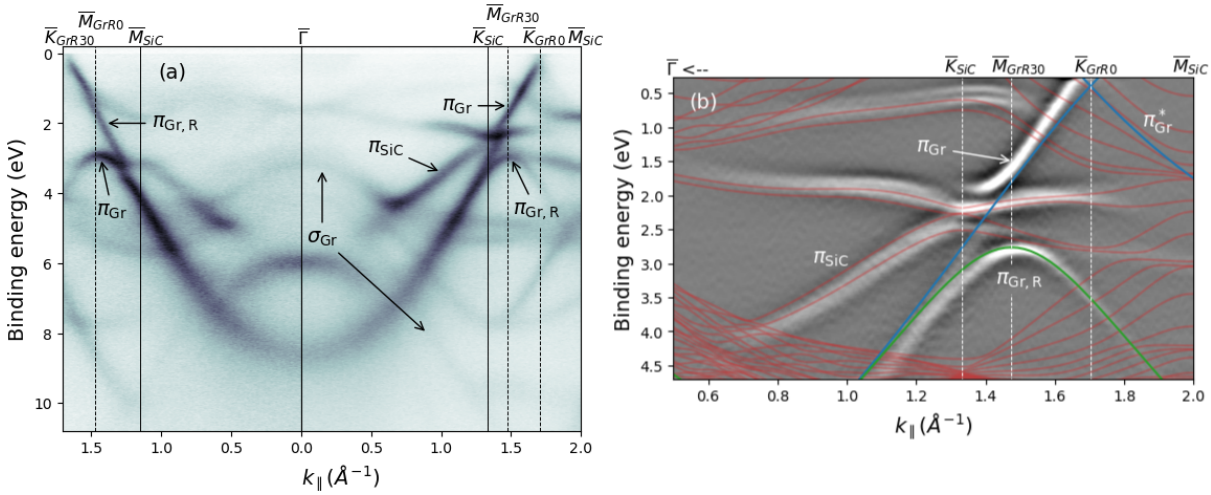

Figure 6.13: (a) Measured band structure of graphene on a SiC monolayer ($h\nu = 100\,\text{eV}$). The graphene bands show two domains, one oriented the same way as the SiC (and TaC), and the other rotated 30°. (b) Higher resolution measurement around the $\overline{K}$-point ($h\nu = 58\,\text{eV}$) with superimposed DFT calculated bands. The blue and green curves show the non-rotated and rotated graphene bands and the red curves show the SiC monolayer bands. The calculated graphene bands are shifted down by 0.4 eV to align the σ bands with the measurement, while the SiC bands are shifted by 0.1 eV to align the Dirac-like crossing at $\overline{K}$.

that the calculated 2D SiC bands were shifted down by 0.1 eV to align the bands at the Dirac-like crossing at $\overline{K}$, resulting in the misalignment of the upper bands, as was observed previously in Section 6.3. With the formation of the SiC monolayer, the graphene π band now intersects the Fermi-level at K, more closely resembling free-standing graphene. Moreover, the calculated graphene bands needed to be shifted down by only 0.4 eV for this sample. This provides further evidence of reduced coupling between graphene and the substrate. Considering that the 2D SiC has no free bonds (they're hybridizing with the TaC surface), this conclusion is reasonable.

In summary, our investigation into the growth process of a SiC monolayer on the TaC(111) surface has provided valuable insights into the growth mechanisms, specifically concerning carbon dynamics. By exposing the sample to ethylene, C is adsorbed onto the surface and then diffuses into the bulk. With continued ethylene exposure, the diffusion of C into the bulk eventually slows down and instead bonds with other C atoms to form graphene. Subsequently, when Si is deposited and the sample annealed, C diffuses back to the surface and bonds with the Si to form a SiC monolayer. When graphene was present, the 2D SiC formed underneath it, resulting in a more freestanding-like graphene.

Chapter 7

Discussion

Previous investigations have consistently reported a charge transfer from tantalum to carbon atoms within the TaC crystal [33,34,107,128,129]. This implies a reduction in the number of electrons available to screen the positively charged tantalum core, increasing the binding energy of the core electrons. As a result, it's reasonable that both the surface and carbon-deficient peaks have lower binding energies. Since they have fewer nearby carbon atoms, less charge transfers from the Ta atoms and the core screening reduces. This charge transfer model also explains why only the surface and stoichiometric bulk C 1s components exist. Despite carbon deficiency impacting the tantalum environment, each carbon atom always maintains its coordination with six tantalum atoms.

A notable discrepancy between the findings in this thesis and prior research lies in the identification of a third peak in the Ta 4f core level, corresponding to carbon-depleted Ta regions. Earlier investigations consistently reported only two peaks [45, 105]. Through fitting of the Ta 4f core level spectrum data presented by Anazawa et al. [45], a more accurate fit was achieved by incorporating a third peak positioned between the surface and bulk peaks. It's worth noting that this additional peak would likely be subtle, particularly given Anazawa et al.'s report of a 0.95 C-Ta molar ratio ($TaC_{0.95}$), indicating few carbon-deficient sites. While this doesn't definitively confirm the presence of a third peak in their data, it underscores the plausibility. The absence of this third peak in earlier studies may be attributed to factors such as lower energy resolution or samples closer to stoichiometry.

Earlier investigations have documented a trend where the Ta 4f core levels shift to lower binding energies with decreasing carbon content and as the crystal approaches lower stoichiometry [33,34]. These studies attributed this shift to a reduction in charge transfer from tantalum to carbon atoms, resulting in a decrease in the Ta 4f binding energy. However, the core level measurements presented in this thesis exhibit no discernible shift in binding energy for the bulk components. Consequently, I propose a hypothesis that challenges the conventional interpretation: the observed shift in binding energy in older and lower resolution measurements may instead reflect changes in the intensities of two bulk components, corresponding to carbon-deficient and stoichiometric Ta sites.

Initial attempts to grow the SiC monolayer directly on the clean TaC(111) surface failed, highlighting a potential barrier caused by carbon deficiency within the TaC crystal. In my work, it became evident that enhancing the crystal's stoichiometry through ethylene exposure was essential for facilitating 2D SiC formation. Despite efforts, achieving complete stoichiometry of the TaC proved difficult, as indicated by the continued existence of the lower binding energy Ta 4f bulk peak. Notably, before reaching stoichiometry, carbon began forming graphene, emphasizing the challenge of precisely controlling the carbon

content at the surface. It appears that while the initial phase of carbon flow into the crystal is fast, the process slows down as carbon vacancies are gradually filled.

Refinement of the ethylene exposure parameters, such as reducing the pressure and extending the duration, offers promise for reaching stoichiometric TaC without causing graphene formation. This strategy may give carbon sufficient time to enter the crystal without bonding to surface C atoms and forming graphene. However, careful consideration must be given to the surface temperature. While a temperature suitable for efficient ethylene cracking is desirable, excessively high temperatures could worsen the escape of carbon into the vacuum, undermining the desired result. Nonetheless, the persistence of the C-depleted Ta 4f bulk peak did not limit SiC monolayer formation, implying that a moderately high C-Ta molar ratio is sufficient.

Chapter 8

Conclusion

This study investigated the growth process of a honeycomb SiC monolayer atop a TaC(111) surface. First, the characterization of the clean TaC(111) crystal revealed that the Ta 4f core level was split into one surface and two bulk components. The presence of a second bulk peak motivated me to study the stoichiometry of the TaC crystal. To do this, carbon was deposited onto the sample via ethylene exposure, which resulted in carbon diffusion into the bulk, filling up C vacancies and thus enhancing the TaC stoichiometry. Subsequently, silicon was deposited and an investigation combining the measured band structure and DFT calculations gave evidence for the formation of a honeycomb SiC monolayer atop the TaC(111) surface. The role of ethylene exposure was essential, as the SiC monolayer could not be formed without additional C deposition. The measured band structure points towards a strong interaction between the SiC monolayer and the TaC substrate.

After proving the SiC monolayer synthesis, the limits of the growth process were explored. By depositing an excess amount of carbon, the formation of graphene atop the TaC(111) surface was observed. Similar to the SiC monolayer, the graphene was found to interact strongly with the substrate. Following the silicon deposition, 2D SiC forms underneath the graphene. ARPES measurements then showed a graphene band structure that more closely resembles freestanding graphene, indicating weaker bonding with the substrate. Moreover, LEED images showed an initially strained graphene lattice that relaxed after the formation of the 2D SiC underneath.

Most importantly, this study demonstrated a new way of growing a SiC monolayer that has better control over the supply of constituent materials. These findings help us understand the mechanisms driving the growth process on the TaC(111) substrate, bringing 2D SiC a step closer to being used in future applications such as transistors or optoelectronic devices.

Chapter 9

Outlook

As I conclude the investigation, I now give an outlook of future research possibilities. One direction is to image the sample surface with a scanning tunneling microscope (STM). It provides high-resolution imaging at the atomic scale, allowing for direct viewing of surface structures and defects. Moreover, STM and scanning tunneling spectroscopy enable the characterization of the electronic properties of the SiC monolayer, such as the local density of electronic states, band gap, and charge distribution.

Studying the behavior of the SiC monolayer under ambient conditions, as well as the feasibility of annealing to restore its pristine state, provides another research opportunity. By subjecting the SiC monolayer to controlled air exposure and varying annealing temperatures, one can examine its stability and determine the threshold temperature to successfully recover the monolayer. Furthermore, investigating the possibility of using graphene as a protective layer could be beneficial. Given graphene's high chemical and thermal stability, it may effectively shield the SiC monolayer from degradation, useful for practical applications. Additionally, studying whether the graphene can function as an electrode on the 2D SiC could prove useful for implementing it into transistors.

Another logical research direction is to try to intercalate a layer underneath the 2D SiC to decouple it from the substrate. Introducing elements like hydrogen, nitrogen, boron, or even alkali metals between the SiC monolayer and the substrate may assist this separation, allowing for independent structural and electronic characterization of the 2D SiC. By detaching it from the underlying TaC crystal, one can investigate its properties with less influence from the substrate, potentially revealing an opening of the band gap at the $\overline{K}$-point, as is predicted by band structure calculations. The next step would be to transfer the SiC monolayer onto a dielectric surface to bring it a step closer to being applied in electronic and optoelectronic devices [130]. Tuning the band gap to fit specific applications such as for light-emitting diodes, lasers, or solar cells could then be done by heterostructuring or doping the SiC monolayer with metal atoms [131].

Investigating the potential for proximity-induced superconductivity in the SiC monolayer is another interesting research direction [132]. With TaC exhibiting superconductivity at relatively high temperatures of 10.3 K [29] and bulk SiC at 1.5 K [133], it raises the question of whether the SiC monolayer can acquire superconductivity through proximity effects. By placing the SiC monolayer near a superconducting material like TaC, researchers could examine whether superconducting behavior emerges in the SiC monolayer at temperatures higher than its bulk counterpart.

Furthermore, the successful formation of a SiC monolayer on the TaC(111) surface provides an opportunity for forming other mono-carbides that have been theoretically

predicted, such as germanium carbide, tin carbide, manganese carbide, and niobium carbide [134–138]. Examining the growth and properties of these mono-carbides expands the scope of two-dimensional carbide research.

I expect that the research and results presented in this thesis will contribute to a future publication.

References

[1] Huang X, Liu C, Zhou P. 2022 2D semiconductors for specific electronic applications: From device to system. *npj 2D Materials and Applications* **6**, 1, 51. (doi:10.1038/s41699-022-00327-3).

[2] Geim AK. 2011 Nobel Lecture: Random walk to graphene. *Reviews of Modern Physics* **83**, 3, 851–862. (doi:10.1103/RevModPhys.83.851).

[3] Chabi S, Kadel K. 2020 Two-Dimensional Silicon Carbide: Emerging Direct Band Gap Semiconductor. *Nanomaterials* **10**, 11, 2226. (doi:10.3390/nano10112226).

[4] Lin X, Lin S, Xu Y, Hakro AA, Hasan T, Zhang B, Yu B, Luo J, Li E, Chen H. 2013 Ab initio study of electronic and optical behavior of two-dimensional silicon carbide. *Journal of Materials Chemistry C* **1**, 11, 2131. (doi:10.1039/c3tc00629h).

[5] Polley CM, Fedderwitz H, Balasubramanian T, Zakharov AA, Yakimova R, Bäcke O, Ekman J, Dash SP, Kubatkin S, Lara-Avila S. 2023 Bottom-Up Growth of Monolayer Honeycomb SiC. *Physical Review Letters* **130**, 7, 076203. (doi:10.1103/PhysRevLett.130.076203).

[6] Keyes RW. 2005 Physical limits of silicon transistors and circuits. *Reports on Progress in Physics* **68**, 12, 2701–2746. (doi:10.1088/0034-4885/68/12/R01).

[7] Liu Y, Duan X, Shin HJ, Park S, Huang Y, Duan X. 2021 Promises and prospects of two-dimensional transistors. *Nature* **591**, 7848, 43–53. (doi:10.1038/s41586-021-03339-z).

[8] Parui S, Ribeiro M, Atxabal A, Llopis R, Casanova F, Hueso LE. 2017 Graphene as an electrode for solution-processed electron-transporting organic transistors. *Nanoscale* **9**, 29, 10178–10185. (doi:10.1039/C7NR01007A).

[9] Gupta S, Sachan R, Narayan J. 2020 Nanometer-Thick Hexagonal Boron Nitride Films for 2D Field-Effect Transistors. *ACS Applied Nano Materials* **3**, 8, 7930–7941. (doi:10.1021/acsanm.0c01416).

[10] Radisavljevic B, Radenovic A, Brivio J, Giacometti V, Kis A. 2011 Single-layer MoS2 transistors. *Nature Nanotechnology* **6**, 3, 147–150. (doi:10.1038/nnano.2010.279).

[11] Manzeli S, Ovchinnikov D, Pasquier D, Yazyev OV, Kis A. 2017 2D transition metal dichalcogenides. *Nature Reviews Materials* **2**, 8, 17033. (doi:10.1038/natrevmats.2017.33).

[12] Liu Y, Huang Y, Duan X. 2019 Van der Waals integration before and beyond two-dimensional materials. *Nature* **567**, 7748, 323–333. (doi:10.1038/s41586-019-1013-x).

[13] Novoselov KS, Mishchenko A, Carvalho A, Castro Neto AH. 2016 2D materials and van der Waals heterostructures. *Science* **353**, 6298, aac9439. (doi:10.1126/science.aac9439).

[14] Geim AK, Grigorieva IV. 2013 Van der Waals heterostructures. *Nature* **499**, 7459, 419–425. (doi:10.1038/nature12385).

[15] Nakamura Y, Yanase Y. 2017 Odd-parity superconductivity in bilayer transition metal dichalcogenides. *Physical Review B* **96**, 5, 054501. (doi:10.1103/PhysRevB.96.054501).

[16] Wang J, Ma F, Liang W, Sun M. 2017 Electrical properties and applications of graphene, hexagonal boron nitride (h-BN), and graphene/h-BN heterostructures. *Materials Today Physics* **2**, 6–34. (doi:10.1016/j.mtphys.2017.07.001).

[17] Ye M, Zhang D, Yap Y. 2017 Recent Advances in Electronic and Optoelectronic Devices Based on Two-Dimensional Transition Metal Dichalcogenides. *Electronics* **6**, 2, 43. (doi:10.3390/electronics6020043).

[18] Illarionov YY, Knobloch T, Jech M, Lanza M, Akinwande D, Vexler MI, Mueller T, Lemme MC, Fiori G, Schwierz F, *et al.* 2020 Insulators for 2D nanoelectronics: The gap to bridge. *Nature Communications* **11**, 1, 3385. (doi:10.1038/s41467-020-16640-8).

[19] Oughaddou H, Enriquez H, Tchalala MR, Yildirim H, Mayne AJ, Bendounan A, Dujardin G, Ait Ali M, Kara A. 2015 Silicene, a promising new 2D material. *Progress in Surface Science* **90**, 1, 46–83. (doi:10.1016/j.progsurf.2014.12.003).

[20] Kharadi MA, Malik GFA, Khanday FA, Shah KA, Mittal S, Kaushik BK. 2020 Review—Silicene: From Material to Device Applications. *ECS Journal of Solid State Science and Technology* **9**, 11, 115031. (doi:10.1149/2162-8777/abd09a).

[21] Şahin H, Cahangirov S, Topsakal M, Bekaroglu E, Akturk E, Senger RT, Ciraci S. 2009 Monolayer honeycomb structures of group-IV elements and III-V binary compounds: First-principles calculations. *Physical Review B* **80**, 15, 155453. (doi:10.1103/PhysRevB.80.155453).

[22] Agarwal AK. 2010 An overview of SiC power devices. In: *2010 International Conference on Power, Control and Embedded Systems*, pp. 1–4. Allahabad, India: IEEE. (doi:10.1109/ICPCES.2010.5698670).

[23] Bekaroglu E, Topsakal M, Cahangirov S, Ciraci S. 2010 First-principles study of defects and adatoms in silicon carbide honeycomb structures. *Physical Review B* **81**, 7, 075433. (doi:10.1103/PhysRevB.81.075433).

[24] Hsueh HC, Guo GY, Louie SG. 2011 Excitonic effects in the optical properties of a SiC sheet and nanotubes. *Physical Review B* **84**, 8, 085404. (doi:10.1103/PhysRevB.84.085404).

[25] Alaal N, Loganathan V, Medhekar N, Shukla A. 2016 First principles many-body calculations of electronic structure and optical properties of SiC nanoribbons. *Journal of Physics D: Applied Physics* **49**, 10, 105306. (doi:10.1088/0022-3727/49/10/105306).

[26] Lin SS. 2012 Light-Emitting Two-Dimensional Ultrathin Silicon Carbide. *The Journal of Physical Chemistry C* **116**, 6, 3951–3955. (doi:10.1021/jp210536m).

[27] Wolfe TA, Jewett TJ, Singh Gaur RP. 2014 Powder Synthesis. In: *Comprehensive Hard Materials*, pp. 185–212. Elsevier. (doi:10.1016/B978-0-08-096527-7.00006-4).

[28] Ghaffari S, Faghihi-Sani M, Golestani-Fard F, Nojabayy M. 2013 Diffusion and solid solution formation between the binary carbides of TaC, HfC and ZrC. *International Journal of Refractory Metals and Hard Materials* **41**, 180–184. (doi:10.1016/j.ijrmhm.2013.03.009).

[29] Shang T, Zhao JZ, Gawryluk DJ, Shi M, Medarde M, Pomjakushina E, Shiroka T. 2020 Superconductivity and topological aspects of the rocksalt carbides NbC and TaC. *Physical Review B* **101**, 21, 214518. (doi:10.1103/PhysRevB.101.214518).

[30] Kempter CP, Nadler MR. 1960 Thermal Decomposition of Niobium and Tantalum Monocarbides. *The Journal of Chemical Physics* **32**, 5, 1477–1481. (doi:10.1063/1.1730944).

[31] Bowman AL. 1961 The variation of lattice parameter with carbon content of tantalum carbide. *The Journal of Physical Chemistry* **65**, 9, 1596–1598. (doi:10.1021/j100905a028).

[32] Yan WL, Sygnatowicz M, Lu GH, Liu F, Shetty DK. 2016 First-principles study on surface stability of tantalum carbides. *Surface Science* **644**, 24–28. (doi:10.1016/j.susc.2015.09.003).

[33] Gruzalski GR, Zehner DM. 1990 Charge-distribution changes accompanying the formation and changes in the composition of HfC x and TaC x. *Physical Review B* **42**, 5, 2768–2777. (doi:10.1103/PhysRevB.42.2768).

[34] Gruzalski GR, Zehner DM. 1986 Defect states in substoichiometric tantalum carbide. *Physical Review B* **34**, 6, 3841–3848. (doi:10.1103/PhysRevB.34.3841).

[35] Zuo JK, Warmack RJ, Zehner DM, Wendelken JF. 1993 Periodic faceting on TaC(110): Observations using high-resolution low-energy electron diffraction and scanning tunneling microscopy. *Physical Review B* **47**, 16, 10743–10747. (doi:10.1103/PhysRevB.47.10743).

[36] Zuo JK, Carpinelli JM, Zehner DM, Wendelken JF. 1996 Scanning-tunneling-microscopy study of faceting on high-step-density TaC surfaces. *Physical Review B* **53**, 23, 16013–16018. (doi:10.1103/PhysRevB.53.16013).

[37] Aono M, Oshima C, Zaima S, Otani S, Ishizawa Y. 1981 Quantitative Surface Atomic Geometry and Two-Dimensional Surface Electron Distribution Analysis by a New Technique in Low-Energy Ion Scattering. *Japanese Journal of Applied Physics* **20**, 11, L829. (doi:10.1143/JJAP.20.L829).

[38] Zaima S, Shibata Y, Adachi H, Oshima C, Otani S, Aono M, Ishizawa Y. 1985 Atomic chemical composition and reactivity of the TiC(111) surface. *Surface Science* **157**, 2-3, 380–392. (doi:10.1016/0039-6028(85)90680-6).

[39] Edamoto K, Abe Y, Ikeda T, Ito N, Miyazaki E, Kato H, Otani S. 1990 Angle-resolved photoemission study of the surface state on NbC(111). *Surface Science* **237**, 1-3, 241–247. (doi:10.1016/0039-6028(90)90535-G).

[40] Souda R, Aizawa T, Otani S, Ishizawa Y. 1990 Effects of chemical bonding on the electronic transition in low energy He+ scattering. *Surface Science* **232**, 1-2, 219–227. (doi:10.1016/0039-6028(90)90601-4).

[41] Fujimori A, Minami F, Tsuda N. 1982 Electronic properties of TiC(100) and polar TiC(111) surfaces. *Surface Science* **121**, 2, 199–217. (doi:10.1016/0039-6028(82)90037-1).

[42] Edamoto K, Anazawa T, Mochida A, Itakura T, Miyazaki E, Kato H, Otani S. 1992 Angle-resolved photoemission study of the surface state on TiC(111). *Physical Review B* **46**, 7, 4192–4197. (doi:10.1103/PhysRevB.46.4192).

[43] Bradshaw A, Van Der Veen J, Himpsel F, Eastman D. 1981 Electronic properties of the clean and hydrogen-covered TiC(111) Ti-terminated polar surface. *Solid State Communications* **37**, 1, 37–40. (doi:10.1016/0038-1098(81)90883-8).

[44] Oshima C, Aono M, Zaima S, Shibata Y, Kawai S. 1981 The surface properties of TiC(001) and TiC(111) surfaces. *Journal of the Less Common Metals* **82**, 69–74. (doi:10.1016/0022-5088(81)90199-5).

[45] Anazawa T, Tokumitsu S, Sekine R, Miyazaki E, Edamoto K, Kato H, Otani S. 1995 Angle-resolved photoemission study of the surface electronic structure of TaC(111). *Surface Science* **328**, 3, 263–268. (doi:10.1016/0039-6028(95)00027-5).

[46] Shi Z, Zhang Z, Kutana A, Yakobson BI. 2015 Predicting Two-Dimensional Silicon Carbide Monolayers. *ACS Nano* **9**, 10, 9802–9809. (doi:10.1021/acsnano.5b02753).

[47] Zhao M, Zhang R. 2014 Two-dimensional topological insulators with binary honeycomb lattices: Si C 3 siligraphene and its analogs. *Physical Review B* **89**, 19, 195427. (doi:10.1103/PhysRevB.89.195427).

[48] Dong H, Wang L, Zhou L, Hou T, Li Y. 2017 Theoretical investigations on novel SiC5 siligraphene as gas sensor for air pollutants. *Carbon* **113**, 114–121. (doi:10.1016/j.carbon.2016.11.029).

[49] Gao ZY, Xu W, Gao Y, Guzman R, Guo H, Wang X, Zheng Q, Zhu Z, Zhang YY, Lin X, *et al.* 2022 Experimental Realization of Atomic Monolayer Si $_9$ C $_{15}$. *Advanced Materials* **34**, 35, 2204779. (doi:10.1002/adma.202204779).

[50] Guo W, Zhao T, Li F, Cai Q, Zhao J. 2023 Si3C Monolayer as an Efficient Metal-Free Catalyst for Nitrate Electrochemical Reduction: A Computational Study. *Nanomaterials* **13**, 21, 2890. (doi:10.3390/nano13212890).

[51] Shu H, Guo J. 2024 Enhanced stability and tunable optoelectronic properties of silicon–carbon monolayers by strain and surface functionalization. *Journal of Materials Chemistry C* **12**, 16, 5916–5925. (doi:10.1039/D4TC00401A).

[52] Ha CV, Ha LT, Hue DT, Nguyen DK, Anh DT, Guerrero-Sanchez J, Hoat DM. 2023 First-principles study of SiC and GeC monolayers with adsorbed non-metal atoms. *RSC Advances* **13**, 22, 14879–14886. (doi:10.1039/D3RA01372C).

[53] Thu Tran HT, Nguyen PM, Van Nguyen H, Chong TV, Bubanja V, Van Vo H. 2023 Atomistic Study of the Bandgap Engineering of Two-Dimensional Silicon Carbide by Hydrogenation. *ACS Omega* **8**, 28, 25424–25431. (doi:10.1021/acsomega.3c02914).

[54] Ren K, Huang L, Shu H, Zhang G, Mu W, Zhang H, Qin H, Zhang G. 2023 Impacts of defects on the mechanical and thermal properties of SiC and GeC monolayers. *Physical Chemistry Chemical Physics* **25**, 47, 32378–32386. (doi:10.1039/D3CP04538B).

[55] Morais WP, Inacio GJ, Amorim RG, Paz WS, Pansini FNN, De Souza FAL. 2023 Topological line defects in hexagonal SiC monolayer. *Physical Chemistry Chemical Physics* **25**, 48, 33048–33055. (doi:10.1039/D3CP04267G).

[56] Singh A, Mahamiya V, Shukla A. 2023 Defect-driven tunable electronic and optical properties of two-dimensional silicon carbide. *Physical Review B* **108**, 23, 235311. (doi:10.1103/PhysRevB.108.235311).

[57] Huang L, Zhai X, Liu H, Gu L, Cui W, Gu X. 2024 Transition metal doped 2D SiC (TM=Ag, Pd and Rh) as a potential candidate for NOx (x = 1,2) and NH3 sensing. *Sensors and Actuators A: Physical* **367**, 115062. (doi:10.1016/j.sna.2024.115062).

[58] Huang L, Gu L, Liu H, Zhai X, Gu X, Wang J. 2024 Tunable electrical and magnetic properties of 2D SiC via adsorption and doping of atmospheric elements (H, C, N, and O). *Physica B: Condensed Matter* **679**, 415809. (doi:10.1016/j.physb.2024.415809).

[59] Jindal R, Roondhe V, Shukla A. 2024 A first-principles study of the electronic, vibrational, and optical properties of planar SiC quantum dots. *Journal of Physics D: Applied Physics* **57**, 6, 065103. (doi:10.1088/1361-6463/ad07b0).

[60] Mélinon P, Masenelli B, Tournus F, Perez A. 2007 Playing with carbon and silicon at the nanoscale. *Nature Materials* **6**, 7, 479–490. (doi:10.1038/nmat1914).

[61] Lü TY, Liao XX, Wang HQ, Zheng JC. 2012 Tuning the indirect–direct band gap transition of SiC, GeC and SnC monolayer in a graphene-like honeycomb structure by strain engineering: A quasiparticle GW study. *Journal of Materials Chemistry* **22**, 19, 10062. (doi:10.1039/c2jm30915g).

[62] Thi Han N, Le Manh T, Khuong Dien V. 2024 Direct correlation between electronic and optical properties of the XC monolayers (X= Si, Ge, and Sn) from first-principles calculations. *Physica E: Low-dimensional Systems and Nanostructures* **159**, 115925. (doi:10.1016/j.physe.2024.115925).

[63] Chabi S, Guler Z, Brearley AJ, Benavidez AD, Luk TS. 2021 The Creation of True Two-Dimensional Silicon Carbide. *Nanomaterials* **11**, 7, 1799. (doi:10.3390/nano11071799).

[64] Susi T, Skákalová V, Mittelberger A, Kotrusz P, Hulman M, Pennycook TJ, Mangler C, Kotakoski J, Meyer JC. 2017 Computational insights and the observation of SiC nanograin assembly: Towards 2D silicon carbide. *Scientific Reports* **7**, 1, 4399. (doi:10.1038/s41598-017-04683-9).

[65] Islam MR, Islam MS, Mitul AF, Mojumder MRH, Islam ASMJ, Stampfl C, Park J. 2021 Superior tunable photocatalytic properties for water splitting in two dimensional GeC/SiC van der Waals heterobilayers. *Scientific Reports* **11**, 1, 17739. (doi:10.1038/s41598-021-97251-1).

[66] Castle JE. 1984 Practical surface analysis by Auger and X-ray photoelectron spectroscopy. D. Briggs and M. P. Seah (Editors). John Wiley and Sons Ltd, Chichester, 1983, 533 pp., £44.50. *Surface and Interface Analysis* **6**, 6, 302–302. (doi:10.1002/sia.740060611).

[67] Bauer E. 1987 G. Ertl, J. Küppers: *Low energy electrons and surface chemistry* , second, completely revised edition, VCH Verlagsgesellschaft, Weinheim 1985. 374 Seiten, Preis: DM 168,-/$ 75.00. *Berichte der Bunsengesellschaft für physikalische Chemie* **91**, 2, 167–167. (doi:10.1002/bbpc.19870910223).

[68] Hüfner S. 2003 *Photoelectron Spectroscopy*. Advanced Texts in Physics. Berlin, Heidelberg: Springer Berlin Heidelberg. (doi:10.1007/978-3-662-09280-4).

[69] Niemantsverdriet JW. 2007 *Spectroscopy in Catalysis: An Introduction*. Wiley, 1 ed. (doi:10.1002/9783527611348).

[70] De Groot F, Kotani A. 2008 *Core Level Spectroscopy of Solids*. CRC Press, 0 ed. (doi:10.1201/9781420008425).

[71] Bluhm H. 2011 X-ray photoelectron spectroscopy (XPS) for in situ characterization of thin film growth. In: *In Situ Characterization of Thin Film Growth*, Woodhead Publishing Series in Electronic and Optical Materials, pp. 75–98. Woodhead Publishing.

[72] Einstein A. 1905 Über einen die Erzeugung und Verwandlung des Lichtes betreffenden heuristischen Gesichtspunkt. *Annalen der Physik* **322**, 6, 132–148. (doi:10.1002/andp.19053220607).

[73] Yao ZQ. 1995 The nature and distribution of nitrogen in silicon oxynitride grown on silicon in a nitric oxide ambient. *Journal of Applied Physics* **78**, 5, 2906–2912. (doi:10.1063/1.360036).

[74] Shirley DA. 1972 High-Resolution X-Ray Photoemission Spectrum of the Valence Bands of Gold. *Physical Review B* **5**, 12, 4709–4714. (doi:10.1103/PhysRevB.5.4709).

[75] Shard AG. 2020 Practical guides for x-ray photoelectron spectroscopy: Quantitative XPS. *Journal of Vacuum Science & Technology A* **38**, 4, 041201. (doi:10.1116/1.5141395).

[76] Major GH, Fairley N, Sherwood PMA, Linford MR, Terry J, Fernandez V, Artyushkova K. 2020 Practical guide for curve fitting in x-ray photoelectron spectroscopy. *Journal of Vacuum Science & Technology A* **38**, 6, 061203. (doi:10.1116/6.0000377).

[77] Schmid M, Steinrück HP, Gottfried JM. 2014 A new asymmetric Pseudo-Voigt function for more efficient fitting of XPS lines. *Surface and Interface Analysis* **46**, 8, 505–511. (doi:10.1002/sia.5521).

[78] Damascelli A. 2004 Probing the Electronic Structure of Complex Systems by ARPES. *Physica Scripta* **T109**, 61. (doi:10.1238/Physica.Topical.109a00061).

[79] Cattelan M, Fox N. 2018 A Perspective on the Application of Spatially Resolved ARPES for 2D Materials. *Nanomaterials* **8**, 5, 284. (doi:10.3390/nano8050284).

[80] Wang K, Ecker B, Gao Y. 2020 Angle-Resolved Photoemission Study on the Band Structure of Organic Single Crystals. *Crystals* **10**, 9, 773. (doi:10.3390/cryst10090773).

[81] Sobota JA, He Y, Shen ZX. 2021 Angle-resolved photoemission studies of quantum materials. *Reviews of Modern Physics* **93**, 2, 025006. (doi:10.1103/RevModPhys.93.025006).

[82] Wikipedia. 2023. Angle-resolved photoemission spectroscopy. `https://en.wikipedia.org/wiki/Angle-resolved_photoemission_spectroscopy`. Accessed: 2024-04-16.

[83] Omicron NanoTechnology. 2002 EA 125 Energy Analyser User's Guide. Tech. Rep. 2.1, Oxford Instruments Group.

[84] Van Hove MA, Weinberg WH, Chan CM. 1986 *Low-Energy Electron Diffraction: Experiment, Theory and Surface Structure Determination*, vol. 6 of *Springer Series in Surface Sciences*. Berlin, Heidelberg: Springer Berlin Heidelberg. (doi:10.1007/978-3-642-82721-1).

[85] Conrad E. 1996 Diffraction Methods. In: *Handbook of Surface Science*, vol. 1, pp. 271–360. Elsevier. (doi:10.1016/S1573-4331(96)80012-6).

[86] Speller S, Heiland W, Schleberger M. 2001 Surface characterization: Composition, structure and topography. In: *Handbook of Surfaces and Interfaces of Materials*, pp. 1–53. Elsevier. (doi:10.1016/B978-012513910-6/50020-7).

[87] Woodruff D. 2002 Low-energy Electron Diffraction. In: *Encyclopedia of Materials: Science and Technology*, pp. 1–4. Elsevier. (doi:10.1016/B0-08-043152-6/01840-4).

[88] Moritz W. 2018 Atomic Structures of Surfaces and Interfaces. In: *Encyclopedia of Interfacial Chemistry*, pp. 55–58. Elsevier. (doi:10.1016/B978-0-12-409547-2.05359-2).

[89] Bauer E. 1994 Low energy electron microscopy. *Reports on Progress in Physics* **57**, 9, 895–938. (doi:10.1088/0034-4885/57/9/002).

[90] Seah MP, Dench WA. 1979 Quantitative electron spectroscopy of surfaces: A standard data base for electron inelastic mean free paths in solids. *Surface and Interface Analysis* **1**, 1, 2–11. (doi:10.1002/sia.740010103).

[91] McRae E, Malic R. 1985 Low energy electron diffraction beam profiles and phase transition at Si(111)-7 X 7 surface. *Surface Science* **161**, 1, 25–32. (doi:10.1016/0039-6028(85)90725-3).

[92] Tucker C. 1964 Low-energy electron diffraction study of CO adsorption on the (100) face of platinum. *Surface Science* **2**, 516–521. (doi:10.1016/0039-6028(64)90094-9).

[93] Anderson J, Danforth W. 1965 Low energy electron diffraction study of the adsorption of oxygen on a (100) Tungsten surface. *Journal of the Franklin Institute* **279**, 3, 160–168. (doi:10.1016/0016-0032(65)90073-6).

[94] Tavares PF, Leemann SC, Sjöström M, Andersson Å. 2014 The MAX IV storage ring project. *Journal of Synchrotron Radiation* **21**, 5, 862–877. (doi:10.1107/S1600577514011503).

[95] Sands M. 1969 The Physics of Electron Storage Rings: An Introduction. *Conf. Proc. C* **6906161**, SLAC-R-121, SLAC-121, 257–411.

[96] Detailed Design Report on the MAX IV Facility. `https://www.maxiv.lu.se/beamlines-accelerators/accelerators/accelerator-documentation-2/`.

[97] Schreiber S. 2014 X-Ray Free-Electron Lasers. In: *Comprehensive Biomedical Physics*, pp. 127–151. Elsevier. (doi:10.1016/B978-0-444-53632-7.00609-2).

[98] Tarawneh H. 2023. Insertion devices. `https://www.maxiv.lu.se/beamlines-accelerators/technology/insertion-devices/`. Accessed: 2023-05-07.

[99] Polley CM. 2023. Beamline optics. `https://www.maxiv.lu.se/beamlines-accelerators/beamlines/bloch/beamline-optics/`. Accessed: 2023-11-16.

[100] Bloch Docs documentation - The Bloch beamline. `https://blochdocs.maxiv.lu.se/beamline.html`.

[101] The Bloch beamline team. 2022 Beamline Review Report. Tech. rep., MAX IV.

[102] Shah A. 2020 *Characterizing the Energy Resolution of Bloch Beamline*. Master's thesis, Lund University, Lund, Sweden. Available at `http://lup.lub.lu.se/student-papers/record/9024713`.

[103] Polley CM. 2023. A-branch measurement chamber. `https://www.maxiv.lu.se/beamlines-accelerators/beamlines/bloch/experimental-station/measurement-chamber/`. Accessed: 2023-11-13.

[104] Polley CM. 2023. Preparation chambers. `https://www.maxiv.lu.se/beamlines-accelerators/beamlines/bloch/experimental-station/preparation-chambers/`. Accessed: 2023-11-13.

[105] Bartynski RA, Yang S, Hulbert SL, Kao CC, Weinert M, Zehner DM. 1992 Surface electronic structure and off-site Auger transitions on TaC(111) observed with Auger-photoelectron coincidence spectroscopy. *Physical Review Letters* **68**, 14, 2247–2250. (doi:10.1103/PhysRevLett.68.2247).

[106] Nyholm R, Martensson N. 1987 N -shell core-level widths for the elements W 74 to Bi 83. *Physical Review B* **36**, 1, 20–24. (doi:10.1103/PhysRevB.36.20).

[107] Greczynski G, Primetzhofer D, Hultman L. 2018 Reference binding energies of transition metal carbides by core-level x-ray photoelectron spectroscopy free from Ar+ etching artefacts. *Applied Surface Science* **436**, 102–110. (doi:10.1016/j.apsusc.2017.11.264).

[108] Powell C, Jablonski A. 2010. NIST Electron Inelastic-Mean-Free-Path Database , SRD 71. (doi:10.18434/T48C78).

[109] Itchkawitz B, Lyman P, Ownby G, Zehner D. 1994 Monolayer graphite on TaC(111): Electronic band structure. *Surface Science* **318**, 3, 395–402. (doi:10.1016/0039-6028(94)90113-9).

[110] Gorham J. 2012. NIST X-ray Photoelectron Spectroscopy Database - SRD 20. (doi:10.18434/T4T88K).

[111] Toneva A, Marinova T, Krastev V. 1998 XPS investigation of a-Si:H thin films after light soaking. *Journal of Luminescence* **80**, 1-4, 455–459. (doi:10.1016/S0022-2313(98)00147-1).

[112] Cerofolini GF, Galati C, Renna L. 2003 Si 2p XPS spectrum of the hydrogen-terminated (100) surface of device-quality silicon. *Surface and Interface Analysis* **35**, 12, 968–973. (doi:10.1002/sia.1632).

[113] Nagashima A, Itoh H, Ichinokawa T, Oshima C, Otani S. 1994 Change in the electronic states of graphite overlayers depending on thickness. *Physical Review B* **50**, 7, 4756–4763. (doi:10.1103/PhysRevB.50.4756).

[114] Presel F, Jabeen N, Pozzo M, Curcio D, Omiciuolo L, Lacovig P, Lizzit S, Alfè D, Baraldi A. 2015 Unravelling the roles of surface chemical composition and geometry for the graphene–metal interaction through C1s core-level spectroscopy. *Carbon* **93**, 187–198. (doi:10.1016/j.carbon.2015.05.041).

[115] Senkovskiy BV, Haberer D, Usachov DYu, Fedorov AV, Ehlen N, Hell M, Petaccia L, Di Santo G, Durr RA, Fischer FR, *et al.* 2017 Spectroscopic characterization of $N = 9$ armchair graphene nanoribbons. *physica status solidi (RRL) – Rapid Research Letters* **11**, 8, 1700157. (doi:10.1002/pssr.201700157).

[116] Wang Y, Zhang Y, Zhang L, Wang Q, Duhm S. 2023 On-Surface Synthesis of Graphene Nanoribbons: Photoelectron Spectroscopy Reveals Impact of Substrate Reactivity. *The Journal of Physical Chemistry C* **127**, 41, 20276–20283. (doi:10.1021/acs.jpcc.3c03194).

[117] Xie W, Weng LT, Ng KM, Chan CK, Chan CM. 2017 Defects of clean graphene and sputtered graphite surfaces characterized by time-of-flight secondary ion mass spectrometry and X-ray photoelectron spectroscopy. *Carbon* **112**, 192–200. (doi:10.1016/j.carbon.2016.11.002).

[118] Ganesan K, Ghosh S, Gopala Krishna N, Ilango S, Kamruddin M, Tyagi AK. 2016 A comparative study on defect estimation using XPS and Raman spectroscopy in few layer nanographitic structures. *Physical Chemistry Chemical Physics* **18**, 32, 22160–22167. (doi:10.1039/C6CP02033J).

[119] Scardamaglia M, Aleman B, Amati M, Ewels C, Pochet P, Reckinger N, Colomer JF, Skaltsas T, Tagmatarchis N, Snyders R, *et al.* 2014 Nitrogen implantation of suspended graphene flakes: Annealing effects and selectivity of sp2 nitrogen species. *Carbon* **73**, 371–381. (doi:10.1016/j.carbon.2014.02.078).

[120] Greczynski G, Hultman L. 2018 Reliable determination of chemical state in x-ray photoelectron spectroscopy based on sample-work-function referencing to adventitious carbon: Resolving the

myth of apparent constant binding energy of the C 1s peak. *Applied Surface Science* **451**, 99–103. (doi:10.1016/j.apsusc.2018.04.226).

[121] Greczynski G, Hultman L. 2020 X-ray photoelectron spectroscopy: Towards reliable binding energy referencing. *Progress in Materials Science* **107**, 100591. (doi:10.1016/j.pmatsci.2019.100591).

[122] Patel DI, O'Tani J, Bahr S, Dietrich P, Meyer M, Thißen A, Linford MR. 2019 Ethylene glycol, by near-ambient pressure XPS. *Surface Science Spectra* **26**, 2, 024007. (doi:10.1116/1.5119256).

[123] Biesinger MC. 2022 Accessing the robustness of adventitious carbon for charge referencing (correction) purposes in XPS analysis: Insights from a multi-user facility data review. *Applied Surface Science* **597**, 153681. (doi:10.1016/j.apsusc.2022.153681).

[124] Susi T, Kaukonen M, Havu P, Ljungberg MP, Ayala P, Kauppinen EI. 2014 Core level binding energies of functionalized and defective graphene. *Beilstein Journal of Nanotechnology* **5**, 121–132. (doi:10.3762/bjnano.5.12).

[125] Rollings E, Gweon GH, Zhou S, Mun B, McChesney J, Hussain B, Fedorov A, First P, De Heer W, Lanzara A. 2006 Synthesis and characterization of atomically thin graphite films on a silicon carbide substrate. *Journal of Physics and Chemistry of Solids* **67**, 9-10, 2172–2177. (doi:10.1016/j.jpcs.2006.05.010).

[126] Virojanadara C, Syväjarvi M, Yakimova R, Johansson LI, Zakharov AA, Balasubramanian T. 2008 Homogeneous large-area graphene layer growth on 6 H -SiC(0001). *Physical Review B* **78**, 24, 245403. (doi:10.1103/PhysRevB.78.245403).

[127] Yang G, Li L, Lee WB, Ng MC. 2018 Structure of graphene and its disorders: A review. *Science and Technology of Advanced Materials* **19**, 1, 613–648. (doi:10.1080/14686996.2018.1494493).

[128] Valvoda V. 1981 X-ray diffraction study of Debye temperature and charge distribution in tantalum monocarbide. *Physica Status Solidi (a)* **64**, 1, 133–142. (doi:10.1002/pssa.2210640114).

[129] Johansson L. 1995 Electronic and structural properties of transition-metal carbide and nitride surfaces. *Surface Science Reports* **21**, 5-6, 177–250. (doi:10.1016/0167-5729(94)00005-0).

[130] Chaves A, Azadani JG, Alsalman H, Da Costa DR, Frisenda R, Chaves AJ, Song SH, Kim YD, He D, Zhou J, *et al.* 2020 Bandgap engineering of two-dimensional semiconductor materials. *npj 2D Materials and Applications* **4**, 1, 29. (doi:10.1038/s41699-020-00162-4).

[131] Li J, Tang Y, Xu S, Lin T, Sun T, Ye H. 2023 Improving Optical and Electronic Performance of Monolayer Silicon Carbide via Metal Doping. In: *2023 24th International Conference on Electronic Packaging Technology (ICEPT)*, pp. 1–4. Shihezi City, China: IEEE. (doi:10.1109/ICEPT59018.2023.10492296).

[132] Li C, Zhao YF, Vera A, Lesser O, Yi H, Kumari S, Yan Z, Dong C, Bowen T, Wang K, *et al.* 2023 Proximity-induced superconductivity in epitaxial topological insulator/graphene/gallium heterostructures. *Nature Materials* **22**, 5, 570–575. (doi:10.1038/s41563-023-01478-4).

[133] Muranaka T, Kikuchi Y, Yoshizawa T, Shirakawa N, Akimitsu J. 2008 Superconductivity in carrier-doped silicon carbide. *Science and Technology of Advanced Materials* **9**, 4, 044204. (doi:10.1088/1468-6996/9/4/044204).

[134] Hantanasirisakul K, Gogotsi Y. 2018 Electronic and Optical Properties of 2D Transition Metal Carbides and Nitrides (MXenes). *Advanced Materials* **30**, 52, 1804779. (doi:10.1002/adma.201804779).

[135] Ji Y, Dong H, Hou T, Li Y. 2018 Monolayer graphitic germanium carbide (g-GeC): The promising cathode catalyst for fuel cell and lithium–oxygen battery applications. *Journal of Materials Chemistry A* **6**, 5, 2212–2218. (doi:10.1039/C7TA10118J).

[136] Marcos-Viquez AL, Miranda Á, Cruz-Irisson M, Pérez LA. 2021 Tin carbide monolayers as potential gas sensors. *Materials Letters* **294**, 129751. (doi:10.1016/j.matlet.2021.129751).

[137] Sheng K, Wang ZY, Yuan HK, Chen H. 2020 Two-dimensional hexagonal manganese carbide monolayer with intrinsic ferromagnetism and half-metallicity. *New Journal of Physics* **22**, 10, 103049. (doi:10.1088/1367-2630/abbf6c).

[138] Zhang B, Huang Y, Bao W, Wang B, Meng Q, Fan L, Zhang Q. 2018 Two-dimensional stable transition metal carbides (MnC and NbC) with prediction and novel functionalizations. *Physical Chemistry Chemical Physics* **20**, 39, 25437–25445. (doi:10.1039/C8CP04541K).